Application of 2D elastic FWI to Rayleigh waves acquired at the Herrenknecht test site

Master's thesis of

Ghazaleh Esmaeilikhansari

at the Geophysical Institute (GPI)
KIT-Department of Physics
Karlsruhe Institute of Technology (KIT)

Date of submission:
29.09.2025

Supervisor:	Prof. Dr. Thomas Bohlen
Co-supervisor:	Prof. Dr. Andreas Rietbrock
Advisor:	Dr. Laura Gassner

Erklärung / Statutory declaration

Ich versichere wahrheitsgemäß, die Arbeit selbstständig verfasst, alle benutzten Hilfsmittel vollständig und genau angegeben und alles kenntlich gemacht zu haben, was aus Arbeiten anderer unverändert oder mit Abänderungen entnommen wurde sowie die Satzung des KIT zur Sicherung guter wissenschaftlicher Praxis in der momentan gültigen Fassung beachtet zu haben.

I declare truthfully that I have written this thesis all by myself, that I have fully and accurately specified all auxiliary means used, that I have correctly cited (marked) everything that was taken, either unchanged or with modification, from the work of others, and that I have complied with the current version of the KIT statutes for safeguarding good scientific practice.

Karlsruhe, 29.09.2025

Signature: Ghazaleh Esmaeilikhansari

Abstract

Elastic full-waveform inversion (FWI) is a physics-based method that can recover quantitative subsurface models by fitting synthetic to observed seismograms. In the near surface, where depths of interest are in the order of tens of meters, Rayleigh waves are the dominant energy in seismic records and carry strong sensitivity to shear-wave velocity. Exploiting this information is particularly valuable for engineering.

The objective of this thesis is to construct a two-dimensional elastic reference model of the Herrenknecht gravel test site in southern Germany. This site serves as the validation ground for the newly developed Urban Vibro Truck (UVT), a mobile seismic vibrator intended for urban geophysical surveys. A reliable near-surface model is essential both for characterizing the test site itself and for calibrating the emitted source signal.

Seismic data were acquired along two perpendicular profiles using hammer blows at 4 m intervals and vertical-component geophones at 1 m spacing. Two alternative starting models were tested: a four-layer model obtained from dispersion-curve inversion and a smooth linear-gradient model. In both cases, elastic 2D FWI converged to consistent solutions. The results reveal a low-velocity zone of approximately 200 m/s within the upper 3–5 m, underlain by a rapid increase to 400–500 m/s and a gradual rise to 600–700 m/s at 16 m depth. These features are consistent across both profiles and at their intersection point, demonstrating the robustness of the inversion.

Multi-parameter tests examined whether compressional velocity (V_p) and density (ρ) could be reconstruct in addition to shear-wave velocity (V_s). While joint inversions achieved similar reductions in data misfit, the V_p and ρ models remained poorly resolved and showed strong parameter trade-offs. In contrast, the V_s-only inversions yielded stable, geologically plausible results.

Overall, the study confirms that Rayleigh-wave-based elastic FWI provides a reliable and reproducible V_s model of the shallow subsurface. This reference model will support future validation of the UVT source and illustrates both the strengths and limitations of Rayleigh-wave FWI in near-surface geophysics.

List of Figures

List of Tables

Contents

Chapter 1

Introduction

The Urban Vibro Truck (UVT) project was initiated to design and validate a novel mobile seismic vibrator for urban geophysical applications. The vibrator is being developed by Herrenknecht GmbH, with field validation conducted by the Geophysical Institute, Karlsruhe Institute of Technology (KIT). A central objective is to characterize and validate the ground force emitted by the vibrator using multiple independent geophysical methods. For this purpose, a well-characterized test site is essential to distinguish source effects from subsurface heterogeneity. An initial characterization was carried out by Rasho (2025), who derived a one-dimensional shear-wave velocity profile and attenuation properties at the Herrenknecht test site using multichannel surface-wave analysis and spectral-ratio techniques. This provided the first quantitative subsurface model for the site and a basis for subsequent inversion studies. The present thesis builds upon this work by extending the characterization to two dimensions using elastic full- waveform inversion (FWI) of Rayleigh-wave data. Dispersion-based 1D methods yield only horizontally averaged profiles, whereas FWI iteratively updates a numerical model to reproduce the entire recorded waveform. This approach has the potential to resolve laterally variable near-surface structures with higher resolution, while also exposing the trade-offs and parameter sensitivities inherent to multiparameter inversion. FWI has emerged as a powerful imaging technique because it exploits the full seismic wavefield, rather than selected arrivals. Although computationally demanding, it can in principle recover high-resolution models of shear-wave velocity (V_s), compressional velocity (V_p) and density (ρ) . In near-surface studies, elastic FWI is particularly valuable because Rayleigh waves dominate shallow recordings and are strongly sensitive to V_s. Whereas conventional processing often discards surface waves as noise, they in fact contain critical information about shallow shear-wave velocities (**foti2018**). The central objective of this thesis is to apply 2D elastic FWI to Rayleigh-wave data acquired at the Herrenknecht test site. Building on the 1D model derived from dispersion analysis, the goal is to recover a higher-resolution 2D model and to evaluate the potential and limitations of multiparameter inversion. The resulting velocity model will support both near-surface characterization and validation of the Urban Vibro Truck source.

1.1 Historical background of full-waveform inversion

The development of full-waveform inversion has been a major advancement in the field of geophysical imaging over the past four decades. Initially proposed in the early 1980s, the method has evolved from conceptual foundations in inverse theory to a sophisticated technique widely used in both academic and industrial applications. This section outlines the historical progression of FWI, particularly focusing on its extension to elastic formulations and its application to Rayleigh waves, which is the foundation of this thesis.

1.1.1 Theoretical foundations and early work

The theoretical basis for FWI can be traced to the seminal work of Tarantola (1984), who formulated seismic inversion as a nonlinear optimization problem. He framed inversion as minimizing the misfit between observed and modeled waveforms. Early studies were restricted to acoustic approximations, but the increasing availability of computational resources facilitated the extension of FWI into elastic and anisotropic domains.

1.1.2 Computational advances and acoustic FWI

During the 1990s, the application of FWI was limited primarily to acoustic media due to computational constraints. Early implementations focused on two-dimensional models and utilized finite-difference methods to simulate wave propagation. Bunks et al. (1995) introduced a multiscale strategy that improved the convergence behavior of the inversion, laying the groundwork for practical field applications. These developments were pivotal in transitioning FWI from theoretical curiosity to a viable imaging tool. However, acoustic formulations ignore shear-wave sensitivity, which limits their applicability in near-surface studies where V_s is the most relevant parameter.

1.1.3 FWI in elastic and anisotropic media

The turn of the millennium saw a growing interest in incorporating elastic and anisotropic effects into FWI to better account for the complexity of real Earth media. Elastic full-waveform inversion (EFWI) allows for the simultaneous inversion of compressional and shear-wave velocities, which is essential in environments where mode conversions and shear-wave effects cannot be neglected. Significant contributions in this area include the work by Virieux and Operto (2009), who provided a comprehensive overview of the theoretical and computational challenges associated with EFWI. Despite these advances, most applications remain focused on deeper exploration settings. Near-surface implementations remain comparatively rare, partly due to cycle-skipping issues and noise sensitivity.

1.1.4 Surface-wave inversion and Rayleigh waves

In the last decade, the application of FWI to surface waves—particularly Rayleigh waves—has garnered increased attention in near-surface geophysics. Traditional methods such as multichannel analysis of surface waves (MASW) (Park et al., 2007) and spatial autocorrelation (SPAC) (Nazarian et al., 1983) have been widely used to extract dispersion curves and invert for one-dimensional shear-wave velocity profiles. However, these approaches often lack lateral resolution and can suffer from inversion non-uniqueness.

FWI in this context improves resolution of V_s and, under favorable conditions, may provide constraints on V_p and ρ. Boaga et al. (2013) and Pan and Wang (2019) demonstrated that elastic FWI of Rayleigh waves can significantly enhance the characterization of shallow subsurface structures, especially when multicomponent data are available. Their findings underscore the value of Rayleigh-wave sensitivity to near-surface shear-wave velocity, making them particularly suitable for engineering and environmental applications.

1.1.5 Practical applications and modern developments

In recent years, elastic FWI has been successfully applied to various field settings, including test sites and urban environments. These implementations have benefited from improved computational techniques, such as frequency-domain solvers, source encoding, and multi-scale inversion strategies. Kalita et al. (2019) introduced a target-oriented FWI approach that focuses computational effort on specific areas of interest, optimizing both performance and resolution.

1.2 Evolution of elastic and multi-parameter FWI

As the method matured, it became clear that different wave types (P-waves, S-waves, and surface waves) contain unique sensitivities to various subsurface properties. This realization led to the development of multi-parameter FWI, in which different physical properties—such as V_p, V_s, and ρ —are simultaneously inverted. The primary challenge in this approach lies in the parameter trade-offs and cross-talk effects due to the different sensitivities and resolutions inherent in the seismic waveforms (Köhn et al., 2012).

Rayleigh waves are most sensitive to V_s, moderately to ρ, and only weakly to V_p (Groos et al., 2017; Wittkamp et al., 2019). This raises a key question: should inversion focus on V_s alone, or attempt to jointly recover V_s, V_p, and ρ despite the risk of trade-offs? In practice, V_s is typically the primary parameter recovered with the highest fidelity. Including ρ can sometimes stabilize the inversion and improve amplitude fitting, but results remain uncertain and prone to trade-offs. Including V_p in Rayleigh-wave inversion remains controversial due to its low sensitivity; however, it may assist indirectly by stabilizing the inversion of other parameters (Wittkamp et al., 2019).

1.2.1 Recent advances in shallow-seismic multi-parameter FWI

Recent work by Groos et al. (2017) and Wittkamp et al. (2019) has demonstrated the feasibility of reconstructing detailed models of V_s and ρ using only Rayleigh waves, particularly in shallow-seismic applications down to 10–20 meters depth. These studies applied full-waveform inversion in the time domain using a viscoelastic wave equation and incorporated multiscale frequency strategies to mitigate the effects of cycle skipping. Although they successfully inverted V_s and ρ , their methods required careful frequency windowing and may not generalize to noisier datasets such as the data acquired at the Herrenknecht test site.

Athanasopoulos et al. (2020) introduced time-frequency windowing techniques in multi-parameter FWI to further reduce parameter coupling and improve resolution. Their results support the notion that with appropriate model parameterization and inversion strategies, reliable multi-parameter reconstructions are achievable even in complex near-surface environments . While previous studies have demonstrated the potential of Rayleigh-wave FWI in controlled or idealized environments, its robustness under real near-surface heterogeneity remains uncertain. In particular, questions remain regarding (i) the stability of multi-parameter inversions, (ii) the reliability of density and P-wave models derived from Rayleigh waves, and (iii) the sensitivity of results to starting models. This study directly addresses these issues at the Herrenknecht test site, which provides a heterogeneous but controlled setting.

1.3 Context of this study

The thesis is organized as follows. Chapter 2 reviews the theoretical background of elastic FWI, emphasizing wave propagation and the challenges of multi-parameter inversion. Chapter 3 presents the field experiment at the Herrenknecht site, describing acquisition geometry, site conditions, and preprocessing. Chapter 4 details the inversion setup and chapter5 show the results for a synthetic test. chapter 6 results, including single- and multi-parameter tests, starting-model sensitivity, and cross-profile consistency. Chapter7 discusses these results in the context of previous studies, highlighting both methodological advances and remaining challenges.

Chapter 2

Theory

2.1 Introduction

Near-surface characterization is essential for applications such as engineering site assessment, environmental studies. In this depth range, seismic surface waves often dominate recorded wavefields, in particular Rayleigh waves. While traditionally treated as noise in exploration seismology, Rayleigh waves contain valuable information about the shallow shear-wave velocity structure, which is the parameter most relevant for geotechnical and geophysical applications (**foti2018**). Full-waveform inversion provides a physics-based framework to exploit this information by directly fitting synthetic waveforms to observed data. In contrast to ray-based methods, FWI uses the complete wavefield, including amplitudes, phases, and converted arrivals, to build high-resolution models. Elastic FWI is particularly suitable for near-surface studies, since it accounts for both compressional velocity (V_p) and shear-waves velocity (V_s) as well as density (ρ), and therefore captures the full complexity of wave propagation. To prepare for this application, this chapter introduces the theoretical framework of elastic FWI. It begins with the physical properties of surface waves, in particular Rayleigh waves, followed by the governing elastic wave equation. Then, the chapter describes forward modeling, misfit definition, and gradient computation using the adjoint-state method. Finally, parameter sensitivity, multiparameter inversion, regularization, and numerical challenges are discussed, providing the theoretical basis for the methodology and results presented in later chapters.

2.2 Surface waves

Seismic waves are commonly divided into body waves, which propagate through the volume of the medium, and surface waves, which travel along the free surface. Among surface waves, Rayleigh waves are of particular importance for near-surface studies because they usually carry the largest fraction of the recorded seismic energy in active-source experiments (Aki and Richards, 2002).

Rayleigh waves arise from the coupling of compressional (P) and vertically polarized shear (SV) motion in the presence of a traction-free boundary. Their particle motion is elliptical in the vertical plane containing the propagation direction, with retrograde motion at the surface and prograde motion at depth (Achenbach, 2012). The amplitude decays exponentially with depth, confining surface waves sensitivity to the upper layers of the subsurface.

In layered media, Rayleigh waves are dispersive: their phase velocity depends on frequency because different wavelengths penetrate to different depths. Low frequencies sample deeper structures, whereas high frequencies are confined to the shallowest layers. This frequency–depth trade-off forms the basis of many surface-wave methods, including multichannel analysis of surface waves (MASW) (Park et al., 2007) and spectral analysis of surface waves (SASW) (Orozco, 2004). In the context of FWI, dispersion is explicitly modeled in the wave equation, allowing Rayleigh waves to be used directly in waveform fitting (**foti2018**).

The sensitivity of Rayleigh waves to elastic parameters is highly unequal. They are most sensitive to the shear-wave velocity V_s, moderately sensitive to density ρ, and only weakly sensitive to compressional velocity V_p (Groos et al., 2017). This makes them particularly effective for constraining V_s models in the near surface, which explains their central role in this study. Since this study focuses on Rayleigh waves, the following sections emphasize their role in shallow-seismic FWI and their sensitivity to multi-parameter inversion.

2.3 Elastic wave equation

The forward and inverse problems in FWI are built upon the elastic wave equation. For an isotropic heterogeneous medium, Newton's second law gives

$$\rho(x,z)\frac{\partial^2 \mathbf{u}}{\partial t^2} = \nabla \cdot \boldsymbol{\sigma} + \mathbf{f}, \tag{2.1}$$

where $\mathbf{u} = [u_x, u_z]^T$ is the displacement vector, ρ is the density, $\boldsymbol{\sigma}$ is the stress tensor, and $\mathbf{f}$ is the external force term.

Stress and strain are related through Hooke's law for isotropic media:

$$\boldsymbol{\sigma} = \lambda(\nabla \cdot \mathbf{u})\mathbf{I} + 2\mu\boldsymbol{\varepsilon}, \tag{2.2}$$

where λ and μ are the Lamé parameters and $\boldsymbol{\varepsilon}$ is the strain tensor (for small strains, $\boldsymbol{\varepsilon} = \frac{1}{2}(\nabla\mathbf{u} + (\nabla\mathbf{u})^{\mathsf{T}})$).

Combining (2.4) with Hooke's law and assuming a *homogeneous* (constant λ, μ, ρ), *isotropic* medium yields the classical second-order Navier equation,

$$\rho\,\frac{\partial^2 \mathbf{u}}{\partial t^2} = (\lambda + \mu)\,\nabla(\nabla\cdot\mathbf{u}) + \mu\,\nabla^2\mathbf{u} + \mathbf{f}, \tag{2.3}$$

or, in index notation for component i,

$$\rho\,\frac{\partial^2 u_i}{\partial t^2} = (\lambda + \mu)\,\partial_i\partial_j u_j + \mu\,\nabla^2 u_i + f_i. \tag{2.4}$$

This form makes the *P–S* decomposition explicit via the divergence and Laplacian operators; it is widely used for time-domain forward modelling in elastic FWI. (For spatially varying parameters, the divergence form (2.4) should be retained to account for parameter gradients.)

The Lamé parameters are related to seismic velocities by

$$V_p = \sqrt{\frac{\lambda + 2\mu}{\rho}}, \qquad V_s = \sqrt{\frac{\mu}{\rho}}. \tag{2.5}$$

Here, V_s plays a dominant role for Rayleigh waves, while V_p and ρ contribute primarily to amplitudes and mode conversions.

The elastic wave equation provides the foundation for numerical forward modeling, which is required to simulate synthetic seismograms and form the basis of inversion.

2.4 Forward modeling

Forward modeling denotes the numerical solution of the elastic wave equation for a given parameterization of the subsurface. In elastic FWI, forward modeling produces synthetic seismograms that enter the misfit functional. The accuracy, stability, and efficiency of the forward solver directly control the quality and reliability of the inversion (Virieux, 1986; Levander, 1988). Finite-difference (FD) methods are widely used for forward modeling in near-surface applications. Velocities and stresses are discretized on staggered grids, with spatial derivatives approximated by centered finite differences (commonly fourth-order) and time integration performed with an explicit leapfrog scheme (Virieux, 1986). Absorbing boundary conditions such as perfectly matched layers (PML) are applied to suppress artificial reflections from model edges (Komatitsch and Martin, 2007). At the free surface, traction-free conditions are imposed, while sources are implemented as body forces or equivalent moment tensors.

The stability of the explicit scheme is controlled by the Courant–Friedrichs–Lewy (CFL) condition (De Moura and Kubrusly, 2013). Grid dispersion is minimized by ensuring at least 10–15 grid points per shortest wavelength. In near-surface studies, where high frequencies and low velocities produce short Rayleigh wavelengths, grid refinement in shallow layers is often required. Attenuation can be included using rheological models such as generalized standard linear solids to better match observed amplitudes (Liu et al., 1976).

Forward modeling thus provides the synthetic data needed to evaluate the misfit, but inversion requires a framework to update the model iteratively. This leads to the formulation of the inverse problem.

2.5 Inverse modeling in full-waveform inversion

The central task of FWI is to estimate subsurface parameters by minimizing the difference between observed and simulated seismic data. Because the relation between seismic wavefields and model parameters is highly nonlinear, FWI is formulated as an iterative optimization problem (Tarantola, 1984; Virieux and Operto, 2009).

At each iteration, the forward problem is solved to generate synthetic seismograms for the current model. These are compared to the observed data through a misfit function. The gradient of the misfit with respect to the model parameters is computed using the adjoint-state method. The model is then updated in the direction that reduces the misfit, and the procedure is repeated until convergence.

2.5.1 Misfit function

The misfit function defines the objective of inversion. In this study, the normalized L_2 norm is used:

$$\mathcal{J}(\mathbf{m}) = \frac{1}{2}\sum_{s=1}^{N_s}\sum_{r=1}^{N_r} \frac{\int_0^T \left\| \mathbf{u}^{\mathrm{obs}}(r,t;s) - \mathbf{u}^{\mathrm{cal}}(r,t;\mathbf{m}) \right\|^2 dt}{\int_0^T \|\mathbf{u}^{\mathrm{obs}}(r,t;s)\|^2 dt}, \tag{2.6}$$

where $\mathbf{m}$ denotes the model vector (e.g., V_s, V_p, ρ), $\mathbf{u}^{\mathrm{obs}}$ is the observed displacement, and $\mathbf{u}^{\mathrm{cal}}$ is the synthetic wavefield. Normalization reduces the sensitivity to absolute amplitudes and makes the inversion more robust to imperfect source or receiver scaling.

2.5.2 Adjoint-state method

Evaluating the gradient of the misfit function with respect to all model parameters directly would be prohibitively expensive. The adjoint-state method provides an efficient alternative by requiring only two wave-equation solutions per source: one forward simulation and one adjoint simulation (Tarantola, 1984; Plessix, 2006).

The forward simulation generates synthetic data and saves wavefields. The difference between observed and synthetic seismograms is then injected at receiver positions as adjoint sources and back-propagated in time. The adjoint and forward wavefields interact to form the gradient:

$$\frac{\partial \mathcal{J}}{\partial m_k} = -\int_0^T \left(\frac{\partial \mathbf{A}(\mathbf{m})}{\partial m_k} \mathbf{u}^{\mathrm{cal}}(t) \right) \cdot \boldsymbol{\lambda}(t)\, dt, \tag{2.7}$$

where $\mathbf{A}(\mathbf{m})$ is the wave operator, m_k a model parameter, and $\boldsymbol{\lambda}$ the adjoint wavefield. Physically, the gradient highlights where changes in the model reduce the data misfit, and can be interpreted as a sensitivity kernel.

2.5.3 Inversion workflow

The adjoint-state method allows FWI to be formulated as an iterative loop:

1. Start from an initial model $\mathbf{m}_0$.
2. Solve the elastic wave equation to compute synthetic data (forward modeling).
3. Compute the misfit $\mathcal{J}(\mathbf{m})$ with observed data.
4. Back-propagate residuals with the adjoint-state method to compute the gradient $\nabla \mathcal{J}$.
5. Update the model parameters $\mathbf{m}$ using an optimization scheme (e.g., steepest descent, conjugate gradient, quasi-Newton).
6. Repeat until convergence criteria are met.

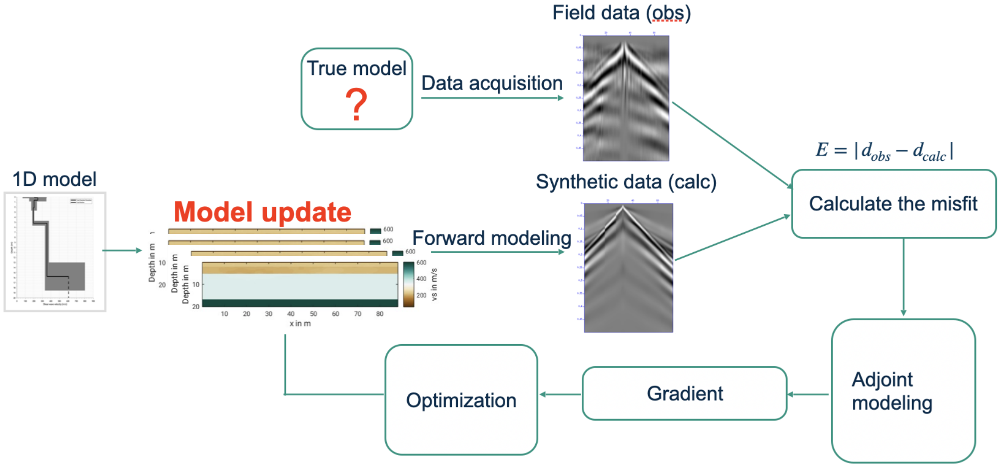

Figure 2.1: *Workflow of the elastic full-waveform inversion (FWI) used in this thesis. Observed field data (*obs*) are compared with synthetic data (*calc*) computed by forward modeling from an initial model. The data residuals are turned into a scalar misfit* $E = \|d_{obs} - d_{calc}\|$*, and adjoint modeling/back-propagation produces the gradient. An optimization step updates the model; the cycle is repeated over successive frequency stages (coarse to fine) until convergence.*

This loop (Figure 2.1) links forward modeling, misfit evaluation, and gradient calculation into a consistent inversion framework. A flowchart of this cycle is often shown to illustrate the conceptual workflow (Virieux and Operto, 2009, see, e.g.,).

2.5.4 Optimization methods

The simplest update strategy is steepest descent:

$$\mathbf{m}_{k+1} = \mathbf{m}_k - \alpha_k \nabla \mathcal{J}(\mathbf{m}_k), \tag{2.8}$$

where α_k is a step length chosen by a line search. While simple, this method converges slowly. More advanced schemes such as nonlinear conjugate gradient or limited-memory BFGS method are often used in practice, as they accelerate convergence by building improved search directions from previous iterations (Nocedal and Wright, 2006).

2.5.5 Multi-parameter inversion

In elastic FWI, the model vector may include shear-wave velocity V_s, compressional velocity V_p, and density ρ. Attempting to recover more than one parameter simultaneously is known as multi-parameter inversion. Although attractive in principle, this approach introduces practical difficulties because of unequal parameter sensitivities and potential cross-talk (Köhn et al., 2012).

For Rayleigh waves, sensitivity studies consistently show the following pattern:

- Strong sensitivity to V_s (dominant control on dispersion and phase velocity).
- Moderate sensitivity to density ρ (mainly through amplitudes and boundary conditions).
- Weak sensitivity to V_p (effects are small in near-surface ranges).

If all three parameters are inverted together, cross-talk can occur, where updates in ρ or V_p mimic the effect of V_s and lead to non-unique solutions. To address this, several strategies are applied:

- **Hierarchical inversion**: start with V_s, then introduce ρ, and only later attempt V_p if supported by the data.
- **Parameter scaling**: rescale gradient amplitudes to balance differences in sensitivity.
- **Regularization**: apply smoothing or damping to stabilize updates of weakly constrained parameters.
- **Data selection**: include body waves or additional amplitude information if V_p or ρ are targeted.

In near-surface Rayleigh-wave FWI, most studies focus primarily on V_s recovery, as it is both well constrained and directly relevant to geotechnical applications (Groos et al., 2013; Groos et al., 2017). Including ρ can improve amplitude fitting but requires careful stabilization, while V_p is rarely resolved reliably without complementary datasets.

2.5.6 Gradient preconditioning

The gradient computed by the adjoint-state method, although exact with respect to the chosen misfit functional, is not directly suitable for model updates. Its amplitude distribution is strongly biased toward shallow structures, where wavefields have the largest energy, and toward parameters with high sensitivity, such as V_s in Rayleigh-wave inversion. Without correction, these imbalances lead to unstable or slow convergence and may cause spurious trade-offs in multiparameter inversion (Plessix, 2006; Virieux and Operto, 2009).

Gradient preconditioning modifies the raw gradient before applying an optimization step in order to improve numerical behavior. Two main approaches are used:

- **Scaling by approximate Hessian (pseudo-Hessian).** The Hessian of the objective function contains information on parameter resolution and sensitivity. Computing it explicitly is prohibitively expensive, but diagonal or block-diagonal approximations can be derived from wavefield amplitudes. A common form is

  $$\tilde{g}_k(\mathbf{x}) = \frac{g_k(\mathbf{x})}{H_{kk}(\mathbf{x}) + \epsilon}, \tag{2.9}$$

  where g_k is the raw gradient for parameter m_k, H_{kk} is an approximate Hessian diagonal (often energy-weighted illumination), and ϵ is a small damping factor. This balances updates across depth and between parameters.
- **Physical-parameter scaling.** When inverting for V_s, V_p and ρ, the raw gradients have different physical units. Rescaling by reference values or by sensitivity norms helps suppress cross-talk. For example, dividing the V_s gradient by $2\rho V_s$ converts it into shear modulus μ, making gradients more comparable (Köhn et al., 2012).

Preconditioning is conceptually distinct from regularization: it does not add prior information, but re-weights the gradient to reflect parameter sensitivities and data illumination. In practice, preconditioning is essential for stable multiparameter inversion in elastic FWI and accelerates convergence even in V_s-only inversions.

2.6 Parameter sensitivity and resolution

Sensitivity kernels quantify how seismic data respond to perturbations in different model parameters. For Rayleigh waves, kernels demonstrate strong sensitivity to V_s in the shallow subsurface, moderate sensitivity to density ρ, and weak sensitivity to V_p (Groos et al., 2017). Depth sensitivity decreases exponentially, with penetration roughly limited to one Rayleigh wavelength.

These unequal sensitivities have direct implications for inversion strategies. Inverting for V_s alone is often stable and effective in near-surface applications. Including ρ can improve amplitude matching but risks introducing parameter trade-offs. Inversions for V_p are generally poorly constrained by Rayleigh waves alone and require additional wave types for reliable recovery.

2.7 Regularization and stabilization

FWI is an ill-posed inverse problem: noise in the data and incomplete coverage lead to non-uniqueness and instability. Regularization introduces additional constraints to stabilize the inversion.

Smoothing constraints penalize rapid variations in the model, suppressing artifacts at wavelengths shorter than those supported by the data. Tikhonov regularization damps large parameter deviations and enforces closeness to the starting model, while total variation regularization preserves sharp contrasts in layered media.

Preconditioning using approximate Hessian information balances updates across depth, while a multiscale inversion strategy—starting from low frequencies and progressively adding higher frequencies—helps avoid convergence to local minima.

2.8 Source-time-function inversion

A fundamental challenge in full-waveform inversion is the correct representation of the source time function (STF), i.e., the temporal signature of the seismic source. In practice, the STF is rarely known exactly: it depends on the source mechanism (hammer, vibrator), coupling conditions at each shot point, and the instrument response. Errors in the STF can be misinterpreted as structural variations in the subsurface, leading to biased inversion results.

To address this, source-time-function inversion (STFI) has been developed and implemented in modern FWI workflows. The basic idea is to treat the STF not as fixed, but as an additional unknown that can be estimated simultaneously with the Earth model (Groos et al., 2014).

2.8.1 Forward problem with unknown STF

The seismogram recorded at a receiver position x_r from a source at x_s can be written as the convolution of the STF $s(t)$ with the Green's function of the Earth $G(x_s, x_r, t)$:

$$g(x_r, t) = \int_0^T G(x_s, x_r, t - t')\, s(t')\, dt'. \tag{2.10}$$

In the frequency domain this becomes

$$g(x_r, \omega) = G(x_s, x_r, \omega)\, s(\omega). \tag{2.11}$$

For the true Earth and the true source, the observed data are

$$d(x_r, \omega) = G_{\text{true}}(x_s, x_r, \omega)\, s_{\text{true}}(\omega). \tag{2.12}$$

The goal of STFI is to estimate the true STF $s_{\text{true}}(\omega)$ given observed data d, synthetic seismograms g, and an initial guess for the STF.

2.8.2 Wiener filter formulation

Introduce a correction filter $c(\omega)$ such that

$$s_{\text{true}}(\omega) \approx c(\omega)\, s(\omega), \tag{2.13}$$

or equivalently

$$d(x_r, \omega) \approx c(\omega)\, g(x_r, \omega). \tag{2.14}$$

Following (Groos et al., 2014), the correction filter can be determined by minimizing a damped least-squares functional:

$$F(c_l; \epsilon) = \sum_{k=1}^{M} f_k^2 \left| d_{lk} - c_l g_{lk} \right|^2 + M \bar{E} \epsilon^2 \left| c_l \right|^2, \tag{2.15}$$

where

- d_{lk} and g_{lk} are the Fourier coefficients of observed and synthetic data at frequency index l and receiver k,
- f_k is an offset-dependent weighting factor,
- M is the number of receivers,
- $\bar{E}$ is an energy normalization factor,
- ϵ is a damping parameter to stabilize against noise.

The analytic solution is obtained by setting $\partial F/\partial c_l = 0$, which yields the Wiener filter:

$$c_l = \frac{\sum_{k=1}^{M} f_k^2 \, g_{lk}^* d_{lk}}{M\bar{E}\epsilon^2 + \sum_{k=1}^{M} f_k^2 \, |g_{lk}|^2}, \tag{2.16}$$

where g_{lk}^* is the complex conjugate of g_{lk}.

The corrected STF is then

$$s_{\mathrm{opt}}(\omega) = c_l \, s(\omega). \tag{2.17}$$

The weighting factor f_k compensates for offset-dependent effects such as geometrical spreading and attenuation:

$$f_k = \left(\frac{r_k}{1\,\mathrm{m}}\right)^{\kappa}, \tag{2.18}$$

where r_k is the source–receiver distance and κ is a scaling exponent. This ensures that traces at different offsets contribute consistently to the estimation of c_l.

The damping term $M\bar{E}\epsilon^2$ stabilizes the inversion and prevents fitting of noise.

2.8.3 Practical aspects

- The initial synthetic wavelet should be broadband (ideally a delta function in time domain) to allow maximum flexibility in correction.
- STF inversion is usually performed once per frequency stage in multiscale FWI, avoiding overfitting.
- The Wiener filter provides a one-step solution, making it efficient and robust.
- A realistic recovered STF is essential for decoupling source errors from model errors, improving convergence and stability (Groos et al., 2014).

2.9 Cycle skipping and challenges

A critical difficulty in FWI is cycle skipping, which occurs when phase differences between observed and synthetic data exceed half a period, leading the inversion to converge toward an incorrect local minimum (Bunks et al., 1995). The multiscale strategy is the most common, but alternative misfit definitions such as traveltime, envelope, or optimal-transport misfits have been proposed to reduce cycle skipping (Luo and Schuster, 1991; Métivier et al., 2018).

Near-surface FWI also faces challenges from limited depth penetration of Rayleigh waves, parameter trade-offs, and high computational costs. These require careful data preprocessing, robust inversion design, and efficient numerical implementation.

2.10 Numerical considerations

FWI is computationally expensive because each iteration requires one forward and one adjoint simulation per source. Memory usage is another constraint: storing the full forward wavefield is impractical, therefore large-scale problems demand parallel computing. Source parallelism distributes different sources across processors, while domain decomposition divides the computational grid itself. Hybrid approaches combine both and are standard in high-performance FWI codes.

Efficient implementation is essential to make elastic FWI feasible for realistic near-surface datasets.

2.11 Summary

This chapter presented the theoretical background of elastic FWI with emphasis on Rayleigh-wave applications in the near surface. The elastic wave equation was introduced as the governing forward problem, followed by its numerical solution using finite differences. The inversion problem was formulated through a normalized L_2 misfit function, and the adjoint-state method was described as the efficient framework for gradient computation.

Rayleigh waves were discussed in detail, highlighting their dispersive properties and unequal parameter sensitivities. These characteristics explain their dominant role in constraining shallow V_s models. Multiparameter inversion strategies and associated trade-offs were considered, together with regularization methods and stabilization techniques such as preconditioning and multiscale inversion. Challenges such as cycle skipping and computational cost were reviewed, underlining the importance of careful design and efficient implementation.

Over all, elastic FWI combines accurate forward modeling, efficient adjoint-based gradients, and stabilization strategies to exploit Rayleigh-wave data for near-surface imaging. This theoretical framework provides the foundation for the methodology and application presented in the following chapters.

Chapter 3

Application to field data

3.1 Data acquisition

The field experiment was conducted on June 20, 2024, at the Herrenknecht test site near Schwanau, Germany, where two 2D seismic profiles were acquired figure 3.2. Profile A (PA) consists of 19 source positions and 72 receivers with a receiver spacing of 1 m, while Profile B (PB) consists of 20 sources and 72 receivers under comparable geometry Figure 3.2.The corresponding coordinates are listed in Table 3.1. A total of five key measurement points (K0–K4) were geolocated with sub-meter accuracy The acquisition layout and control points K0–K4 are shown in Figure 3.1.

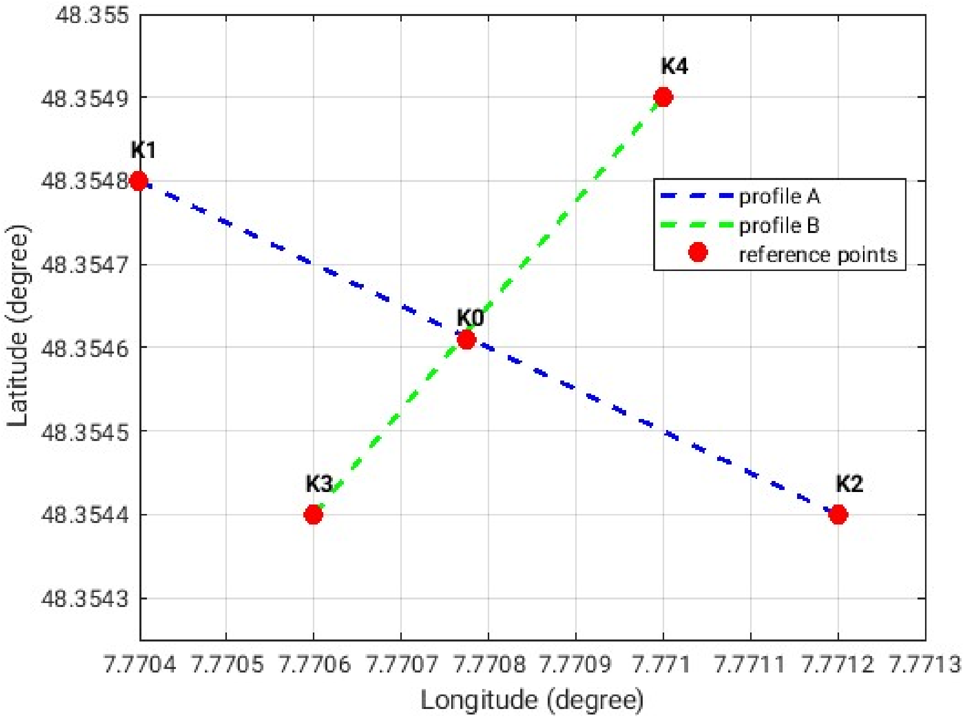

Figure 3.1: *Acquisition geometry at the Herrenknecht test site. Dashed lines indicate Profile A (blue) and Profile B (green). Red markers denote control points K0–K4 used for positioning. Axes show WGS84 latitude and longitude in degrees.*

The seismic source was a hammer blow, producing records dominated by dispersive Rayleigh

Table 3.1: *Reference coordinates for data acquisition (determined using Google Maps)*

Coordinate	Latitude	Longitude
K0	48.354667	7.770843
K1	48.354826	7.770413
K2	48.354472	7.771282
K3	48.354401	7.770624
K4	48.354974	7.771089

waves and first arrivals. These wave types provide complementary sensitivity: Rayleigh waves constrain shear-wave velocity variations in the shallow subsurface, whereas first arrivals help stabilize the long-wavelength velocity structure. The datasets therefore evaluating elastic full-waveform inversion (FWI) strategies in the near-surface regime.

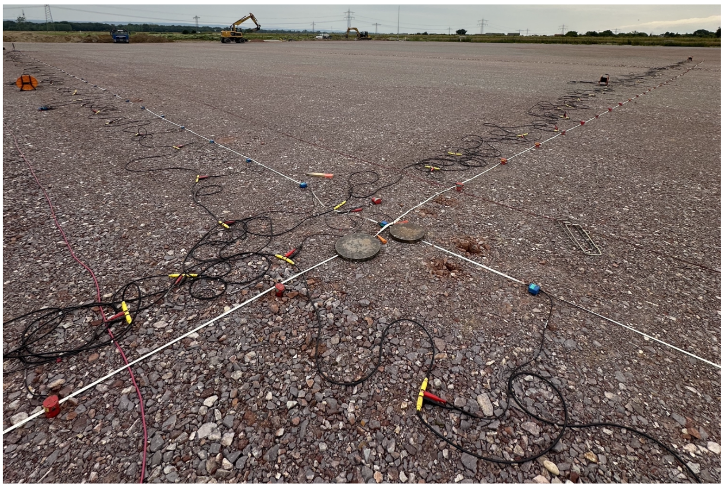

Figure 3.2: *Field view at the profile intersection near K0. White tapes mark the two survey lines; geophones are spaced at 1 m with visible cabling. This photo documents the layout and surface conditions during acquisition. Source: Rasho (2025).*

The terrain consists of compact, layered soils, with stratigraphy characterized by:

- **Top layer:** red gravel, approximately 20 cm thick,
- **Middle layer:** clay-rich soil extending to about 1 m,
- **Bottom layer:** coarse gravel with large stones beyond 1 m depth.

These subsurface conditions pose a challenge for wave propagation, particularly due to heterogeneities caused by large boulders Figure 3.3.

Because of the hard ground, each receiver hole was pre-drilled with a 6 cm auger. Along profile B, a drainage trench required minor relocations to geophones (positions around 7.0, 8.0, and 10.3 m). One data file (`15.dat`) was noted as potentially incomplete and flagged for review during preprocessing. that's the season we have 19 shots in profile A.

3.1.1 Source configuration and recording

Sources were fired every 4 m, starting 1 m behind the first geophone. At each position, ten blows were stacked to improve signal-to-noise ratio. Data were recorded to SEG-2 format on a laptop stationed at K0.

Figure 3.3: *Drainage trench at the test site, exposing the near-surface stratigraphy: a thin red-gravel cap over clay-rich soil and underlying coarse gravel with large stones. The trench led to small receiver relocations. Source: Rasho (2025).*

3.2 Initial subsurface model

A crucial component in full-waveform inversion (FWI) is the selection of a suitable initial velocity model. The convergence behavior and reliability of the inversion are highly dependent on how accurately the initial model approximates the true subsurface structure. To reduce the risk of cycle skipping, the starting model must capture the large-scale velocity trends, even if fine-scale features are absent.

In this study, the initial shear wave velocity model (V_s) was constructed by inversion of dispersion curves (Figure 3.4). It was derived by Rasho (2025) from the data set which was aquired at Herrenknescht test site in Germany. The model represent a horizontally layered subsurface, increasing in velocity with depth. It includes three main layers:

- **Layer 1:** A soft surface layer with V_s = 150–200 m/s, extending to a depth of 0.5 m.
- **Layer 2:** An intermediate soil layer with V_s = 300–400 m/s, extending to 2 m depth.
- **Layer 3:** A consolidated or gravel-rich base layer with V_s increasing linearly to 600–800 m/s down to 5 m depth.

No significant lateral variation was included in the starting models used in chapter 6, as the objective was to emphasize vertical structure suitable for Rayleigh-wave analysis. These 1D model figure 3.4was then extended laterally into a 2D model, serving as the baseline for all inversions. For V_p and ρ, constant values were assumed:

- $V_p = 1440$ m/s throughout,
- $\rho = 1880$ kg/m^3.

Because surface waves are relatively insensitive to these parameters. The chosen values represent partially consolidated, saturated silty sand to soft clay and were applied uniformly across layers in the initial model. These simplifications follow the findings of Groos et al. (2013), who demonstrated that Rayleigh wave sensitivity to V_p and ρ is significantly lower than to V_s. Thus, fixing these parameters helps reduce inversion instability without substantially impacting the result.

The initial model was discretized on a regular grid matching the finite-difference forward model configuration.

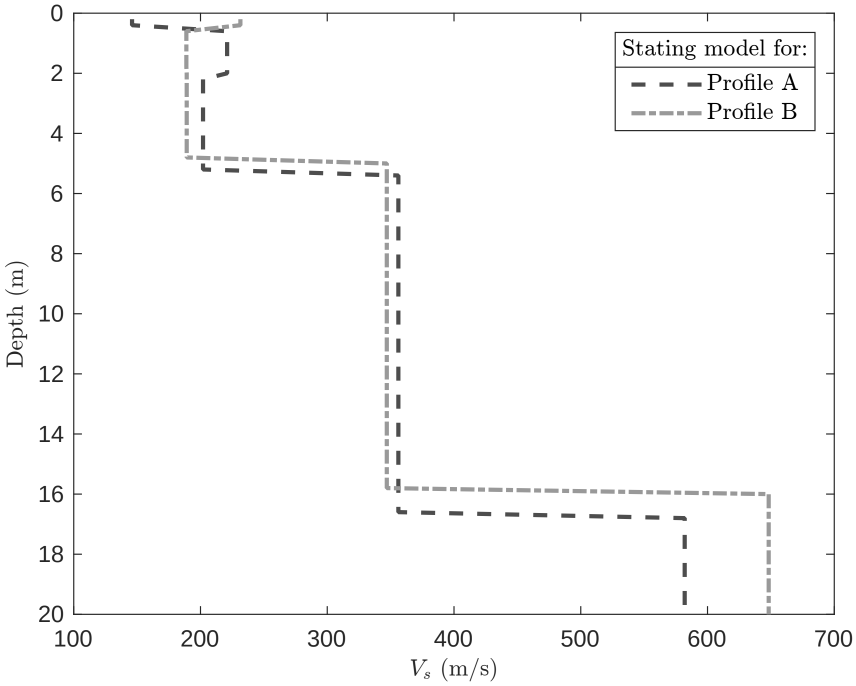

Figure 3.4: *Starting models were derived from the inversion of dispersion curves. The dashed dark-gray and light-gray curves represent the initial* V_s *models obtained by inverting Rayleigh-wave dispersion curves for Profiles A and B, respectively. After extending these models, they were used as the initial parameterizations for the 2D FWI.*

3.2.1 Raw shot gathers

Representative raw vertical-component shot gathers from both profiles are shown in figures 3.5 and 3.6, prior to any filtering or preprocessing. Each panel displays the first, a central, and the last shot along each profile. The records are dominated by the dispersive Rayleigh wavetrain; first arrivals are visible but weaker. Last shots show one-sided moveout, whereas the central shot is nearly symmetric about the source position. Profile A exhibits slightly stronger lateral variability in amplitude and moveout than Profile B, consistent with the geological differences discussed later. These characteristics motivated the preprocessing choices in Sec. 3.3: band-pass filtering to 5–70 Hz, time-windowing to the Rayleigh-wave train, and root-mean-square (RMS) normalization per gather to reduce source/coupling variability.

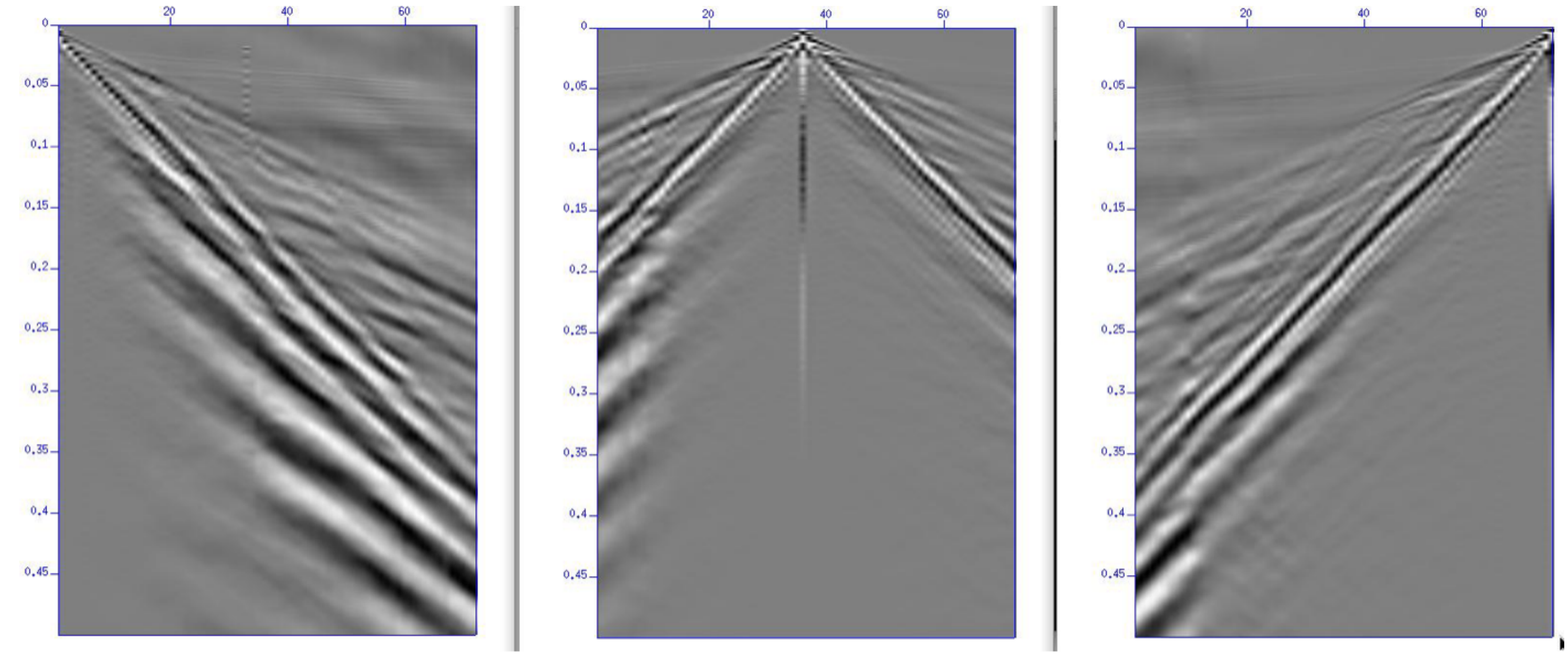

Figure 3.5: *Raw vertical-component shot gathers from* ***Profile A****. Panels (a)–(c) show, respectively, the first shot at one end of the line, a central shot near the profile midpoint, and the last shot at the opposite end. Time increases downward and offset along the top axis increases left to right. The records are dominated by the dispersive Rayleigh wavetrain; the central panel is nearly symmetric around the source position, while the end-on shots show the expected one-sided moveout. Subtle amplitude/moveout changes along the line hint at mild lateral variability.*

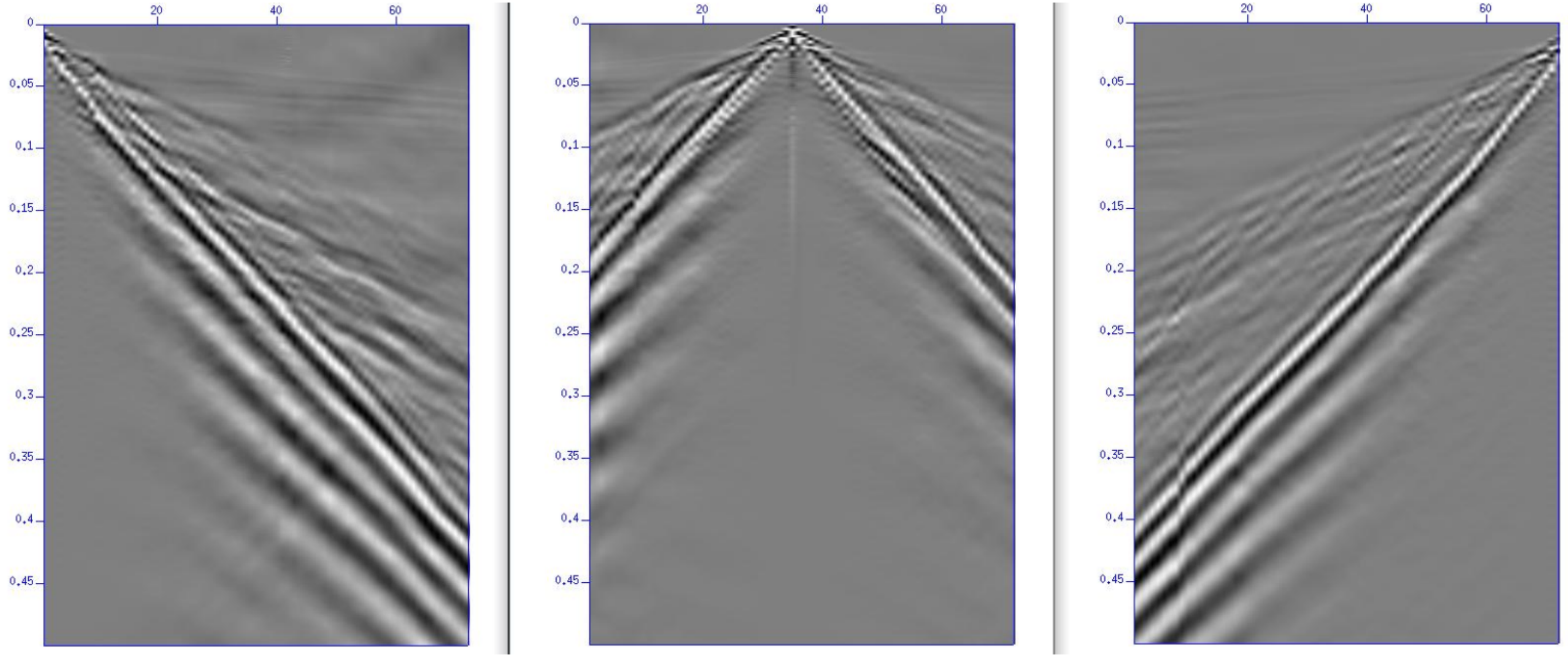

Figure 3.6: *Raw vertical-component shot gathers from* ***Profile B****. Panels (a)–(c) display the first shot, a central shot, and the last shot. As in Profile A, the fundamental Rayleigh mode is the dominant arrival and forms a clear dispersive wavetrain. Compared with Profile A, the gathers appear more laterally homogeneous, with smoother amplitude patterns and fewer localized variations, consistent with the interpretation of weaker lateral changes along this profile.*

3.3 Preprocessing

The raw field records acquired at the Herrenknecht test site required careful preprocessing before entering the inversion workflow. The goals of preprocessing were to (i) improve signal-to-noise ratio (SNR), (ii) isolate the Rayleigh-wave energy that provides the primary sensitivity to V_s, and (iii) ensure compatibility between observed and synthetic data. The following steps were applied sequentially: source stacking, trace inspection and editing, frequency filtering, amplitude normalization, and geometry verification.

- At each shot position, ten hammer blows were recorded and stacked to enhance the SNR. Stacking N independent shots improves SNR approximately by $\sqrt{N}$; for $N = 10$ this corresponds to a factor ~ 3.2. The stacked gathers were used as the input dataset for all subsequent preprocessing and inversion steps.
- All receivers were visually inspected for spurious amplitudes, dropouts, and timing inconsistencies. One record shot 15 was flagged in the field as potentially incomplete and was excluded from further processing. In addition, minor deviations from linearity introduced by receiver relocations.

3.3.1 Amplitude normalization

Amplitude variability remained after stacking due to slight differences in hammer impacts and receiver coupling. To stabilize the inversion against these effects, each shot gather was normalized by the RMS amplitude of its Rayleigh window. This approach preserves relative amplitude information within a gather while minimizing the influence of source strength fluctuations. It is consistent with the time-windowed L_2 misfit used in the inversion (Chapter 4).

Chapter 4

Inversion setup

4.1 Introduction

The inversion of the two datasets (Chapter 3) was carried out with the open-source code IFOS2D (Inversion of Full Observed Seismograms), which implements a viscoelastic time-domain full-waveform inversion (FWI) based on the staggered-grid finite-difference (FD) method (Virieux, 1986; Levander, 1988). This section details the numerical modeling environment, boundary conditions, Source time function estimation, viscoelastic attenuation, inversion parameters, optimization strategy, and computational setup. A careful configuration of these elements is essential to achieve stable and geophysically meaningful inversion results. A machine-readable JSON configuration file (IFOS2D settings) accompanying this chapter is provided in Appendix B.1.

4.1.1 Numerical grid and discretization

Forward modeling in IFOS2D is based on the stress–velocity formulation of the elastic wave equation (Eq. 2.4) discretized on a standard staggered grid (SSG). Velocities and stresses are located at half-grid offsets to improve accuracy and stability (Virieux, 1986). Material properties (V_p, V_s, ρ) are placed at integer grid nodes, while velocity components (v_x, v_y) and shear stress (σ_{xy}) are defined at staggered positions. This configuration avoids oscillations and guarantees accurate representation of wave propagation.

The spatial grid spacing Δh must satisfy the dispersion criterion

$$\Delta h \leq \frac{V_{\min}}{n f_{\max}}, \tag{4.1}$$

where $V_{\min}$ is the minimum velocity in the model, $f_{\max}$ the maximum frequency considered, and n the number of grid points per minimum wavelength. Following the recommendations of Köhn et al. (2012) and the IFOS2D manual, $n = 8$–10 with fourth-order Holberg-optimized FD operators, yielding an accurate representation of the surface-wave field while maintaining feasible computational cost.

Temporal discretization is constrained by the Courant–Friedrichs–Lewy (CFL) stability condition (De Moura and Kubrusly, 2013)

$$\Delta t_i \leq \frac{\Delta h}{h\sqrt{2}V_{\max}}, \tag{4.2}$$

where $V_{\max}$ is the maximum velocity in the model and h a factor depending on the FD operator order (for 4th-order Holberg operators, $h \approx 1.18$). The time step Δt was chosen conservatively to ensure numerical stability during forward and adjoint simulations.

The computational domain was discretized on a uniform staggered grid with 440×100 nodes in the horizontal and vertical directions, respectively, and a grid spacing of $\Delta h = 0.2$ m. This corresponds to a physical model size of approximately 88×20 m, which comfortably covers the geophone spread (72 m aperture) and extends in depth to one to two dominant Rayleigh wavelengths.

Spatial derivatives were approximated with fourth-order finite-difference operators, as recommended by Levander (1988) for accuracy with surface waves. The time integration used an explicit leapfrog scheme with a fixed time step of $\Delta t = 5 \times 10^{-5}$ s (50 μs). This choice satisfies the Courant–Friedrichs–Lewy (CFL) stability criterion for the maximum velocity and ensures at least 8–10 grid points per minimum wavelength within the highest frequency band (up to 70 Hz). The total simulated time was 0.5 s per shot, sufficient to capture the dispersive Rayleigh wavetrain.

Parallelization was carried out by domain decomposition into 8×5 subdomains, resulting in 40 message passing interface (MPI) processes.

4.1.2 Boundary conditions

A traction-free surface boundary condition was applied at the top of the model to allow realistic propagation of Rayleigh waves. Along the lateral and bottom boundaries, perfectly matched layers (PML) of thickness 10 grid points were implemented to suppress artificial reflections. The PML parameters included a reference velocity of 1700 m/s, a reference frequency of 31.25 Hz, power exponent $n = 4$, and maximum damping coefficient $k_{\max} = 1.0$. Tests confirmed that these settings effectively absorbed outgoing wave energy within the inversion frequency range.

4.1.3 Source time function estimation

Accurate characterization of the seismic source is essential for reliable FWI. In IFOS2D, we enable STF inversion via a parameter flag (`INV_STF` = 1), estimating the source wavelet coefficients alongside subsurface velocities, which reduces mismatch due to imperfect source characterization. STF inversion mitigates the instrumental imprint of the hammer blow and enhances model fidelity. Groos et al. (2017) demonstrated that incorporating source-wavelet correction significantly reduces inversion artefacts when using unknown or complex sources. By jointly inverting STF and subsurface parameters through a stabilized least-squares approach, our methodology follows best practices to isolate Earth structure from source effects and improve convergence—especially within a multistage frequency strategy.

Each shot was modeled as a vertical point force (`SOURCE_TYPE` = 3) applied at the free surface, consistent with the hammer source used in the field. The source time function was an Ormsby wavelet read from an external file (`ormsby.dat`), with corner frequencies chosen to match the measured hammer spectrum. All source positions were read from the acquisition file, and multiple shots were run sequentially.

For completeness, the full set of stage-by-stage STFI diagnostics is given in Appendix A.

4.1.4 Viscoelastic attenuation

Intrinsic attenuation was modeled with a three-standard-linear-solid (SLS) rheology using relaxation frequencies at 0.52, 7.67, and 72.7 Hz with a relaxation time constant $\tau = 0.0966$ s. This parameterization ensures realistic amplitude decay across the inversion frequency band (5–70 Hz) and avoids overestimation of coda energy. The inclusion of attenuation is particularly important in the near surface, where scattering and intrinsic losses are strong.

4.1.5 Inversion parameters

The inversion was configured for a maximum of 400 iterations (`ITERMAX`=400). Only the shear-wave velocity V_s was inverted, starting from the first iteration (`INV_VS_ITER`=0). Compressional velocity V_p and density ρ were kept fixed at their initial values until iteration 400, effectively excluding them from the inversion in monoparameter inversion. This choice reflects the strong sensitivity of Rayleigh waves to V_s and the weak sensitivity to V_p and ρ (see Section 1.6).

The misfit was defined as the normalized L_2 norm (`LNORM`=7), evaluated every 15 time steps (`DTINV`=15). Normalization was disabled (`NORMALIZE`=0), relying instead on preprocessing and source-time function inversion to handle amplitude scaling. The adjoint wavefield was computed using adjoint type 2 (`ADJOINT_TYPE`=2), which corresponds to classical adjoint sources at the receiver positions. A complete list of all parameter keys and values used in the runs is given in Appendix B.1.

4.1.6 Frequency filtering(Multi-scale approach)

A multiscale frequency continuation strategy was employed. The inversion started with a low-pass cutoff at 5 Hz and progressively increased the cutoff in 10 Hz increments up to 70 Hz. At least 10 iterations were run per frequency stage (`MIN_ITER`=10). This strategy reduces cycle skipping by fitting long wavelengths first and introducing shorter wavelengths only after large-scale structures are recovered.

4.1.7 Regularization and stabilization

To stabilize the inversion, several measures were implemented:

- **Model smoothing:** after each update, the velocity model was filtered with a 3-point Gaussian kernel (`MODEL_FILTER=1`, `FILT_SIZE=3`) to suppress grid-scale oscillations.
- **Gradient tapering:** a circular taper of radius 3 grid points was applied around each source position (`SRTRADIUS=3`) to reduce near-source artifacts in the gradient.
- **Parameter bounds:** V_s was constrained to remain within 100–5000 m/s, V_p within 100–2420 m/s, and ρ within 0–5000 kg/m^3.
- **Trace killing:** traces within 0–5 m offset from the source were excluded from the misfit calculation using a trace-kill file, in order to suppress near-field effects not modeled by the elastic approximation.

4.1.8 Optimization strategy

The inversion used a nonlinear conjugate-gradient (NCG) method (`GRAD_METHOD`=1) with Wolfe conditions (`WOLFE_CONDITION`=1) to ensure robust line searches. Step lengths were limited to a maximum factor of 4 (`STEPMAX`=4), with scaling parameter $\epsilon = 0.04$. A parabolic fit was used for line search trials, and five Wolfe tests were performed per iteration. For comparison, a limited-memory BFGS option was available but not used systematically in this study.

The stopping criterion was a relative misfit reduction of 0.2% (`PRO`=0.002) between successive iterations, or a maximum of 400 iterations.

4.1.9 Computational setup

All inversions were run in parallel using MPI domain decomposition on 40 processes (8×5). A single forward or adjoint simulation (440 × 100 grid, 72 receivers, 19 sources) required approximately a few minutes on a standard multi-core cluster node. Each iteration of the

Table 4.1: *Summary of inversion parameters used in this study. A machine-readable JSON configuration is provided in Appendix B.1.*

Category	**Setting**
Grid	440×100 nodes, $\Delta h = 0.2$ m, domain $\approx 88 \times 20$ m
FD order	4 (Holberg operators)
Time stepping	$\Delta t = 5 \times 10^{-5}$ s, total time 0.5 s
Parallelization	8×5 subdomains (40 MPI processes)
Boundary conditions	Free surface at the top; PML (10 grid points) sides and bottom
Source	Vertical force, Ormsby wavelet
Receivers	72 vertical geophones, 1 m spacing
Attenuation	3 SLS, f_L =0.52, 7.67, 72.7 Hz, $\tau = 0.0966$ s
Inverted parameters	V_s only (from iteration 0); V_p, ρ fixed
Iterations	Up to 400
Misfit function	Time-windowed L_2 norm (LNORM=7)
Frequency stages	5–70 Hz, increments of 10 Hz, min. 10 iterations per stage
Regularization	Model smoothing (3-point), gradient taper (r=3), parameter bounds
Trace killing	Offsets 0–5 m excluded
Optimization	Nonlinear conjugate gradient, Wolfe line search, STEPMAX=4
Termination	Misfit reduction $< 0.2\%$ or 400 iterations

inversion involved one forward and one adjoint run per source, resulting in about one hour per iteration cycle. A full inversion (400 iterations across all frequency stages) required several hundred core hours. Wavefield checkpointing was not used; instead, recomputation was employed for gradient formation, trading additional runtime for reduced memory demand.

Chapter 5

Synthetic test results

5.1 Introduction

To better understand the performance and limitations of multi-parameter full-waveform inversion in the near surface, a controlled synthetic test was performed. The dataset consists of **40 receivers** and **5 sources**, generated for a simple two-layer elastic model. The inversion setup was identical to that used for the field data, allowing direct comparison of results. A multiscale frequency strategy with **four stages** was applied, with the following maximum frequencies: 10, 20, 40, and 80 Hz. This progression ensures that long-wavelength features are recovered first, before higher frequencies introduce finer structure, thereby reducing the risk of cycle-skipping. Four inversion parameterizations were tested:

1. V_s only,
2. V_s and V_p,
3. V_s and ρ,
4. V_s, V_p and ρ.

The starting and true models used in the experiment are summarized in Table 5.1. The starting model consists of a shallow low-velocity zone with velocities and density increasing with depth, and V_s was constrained to remain within 100–5000 m/s, V_p within 100–2420 m/s, and ρ within 0–5000 kg/m^3. The true model differs slightly in having lower shallow velocities and higher density at depth.

Table 5.1: *Starting and true model parameters for the synthetic test.*

Model	Depth (m)	ρ (kg/m^3)	V_p (m/s)	V_s (m/s)
Starting	0	1720	427	130
	9	1980	1700	285
Starting	0	1720	427	130
	15	1980	1700	285
True	0	1703	357	92
	9	2001	1745	275
True	0	1703	357	92
	15	2001	1745	275

5.2 1D profiles

To evaluate the sensitivity more directly, 1D profiles were extracted at an offset of 20 m (dashed blue line in Figure 5.3) and are shown in Figure 5.4. These profiles allow a direct comparison between the V_s-only inversion and the multi-parameter inversion.

- **V_s:** The three-parameter inversion (V_s, V_p and ρ) yields the V_s profile closest to the true model, especially in the 0–10 m range. Including ρ helps align V_s more closely with the target.
- **ρ:** Despite its role in improving the V_s recovery, the inverted ρ profiles are far from the true density model. This reflects the weak and indirect sensitivity of Rayleigh waves to density.
- **V_p:** The V_p profiles remain close to the starting values, and reasonably close to the true model, but their variations are small and not robust.

5.3 Misfit evolution

The misfit curves (Fig. 5.1) confirm the findings mentioned in section 5.2. A multi-scale approach is used, and in this case we have 4 FWI stages, and the frequency bands are 10, 20, 40, and 80 Hz.

- The misfit decreases in stages as the maximum frequency band is progressively increased. At the beginning of each stage, the introduction of higher frequencies causes a temporary jump in misfit, which then decreases as the inversion iterates. The lowest final misfit is obtained for the three-parameter inversion (V_s, V_p and ρ). However, the final misfit values of the three-parameter inversion and the two-parameter inversion (V_s–V_p) are very similar
- The V_s and ρ case yields similar misfit reductions as V_s-only, showing that density updates alone do not provide a significant improvement.
- Importantly, misfit reduction does not necessarily indicate better parameter recovery: the inversion distributes residuals among V_s, V_p, and ρ, but only the V_s structure is reliably constrained.

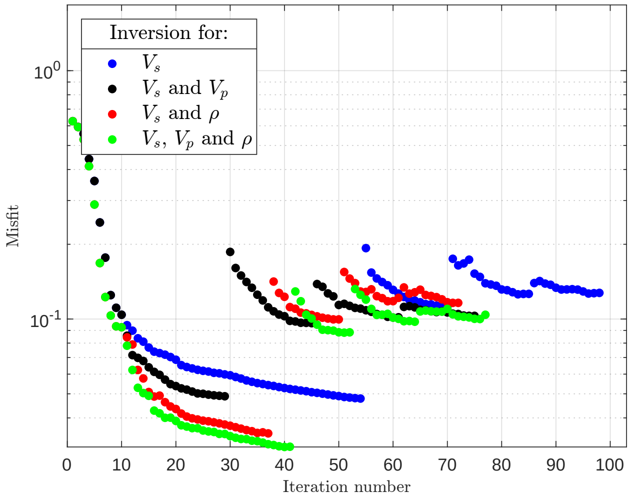

Figure 5.1: *Misfit evolution for synthetic inversions. Blue circles: V_s-only; black: V_s and V_p; red: V_s and ρ; green: V_s, V_p and ρ.The three-parameter inversion (V_s,V_p and ρ) achieves the lowest misfit, but this does not guarantee reliable recovery of ρ or V_p.*

5.4 Data fit

Direct comparison of observed and synthetic seismograms provides the most meaningful validation of the inversion. All seismograms are compared at the final stage (FWI stage 4, 80 Hz) and the last iteration (Fig. 5.2). Observed and synthetic seismograms shows that the main dispersive features of the Rayleigh wavefield are already well reproduced by the V_s-only inversion. Additional parameterizations ($V_s and V_p$, $V_s and \rho$ and $V_s, V_p and \rho$) produce only minor improvements, primarily in waveform amplitudes, while phase alignment remains largely unchanged. The difference between the $V_s and V_p$ and $V_s, V_p and \rho$ inversions is particularly small and difficult to distinguish in the data fit, confirming that the sensitivity of Rayleigh waves to V_p and ρ is weak compared to their strong dependence on V_s.

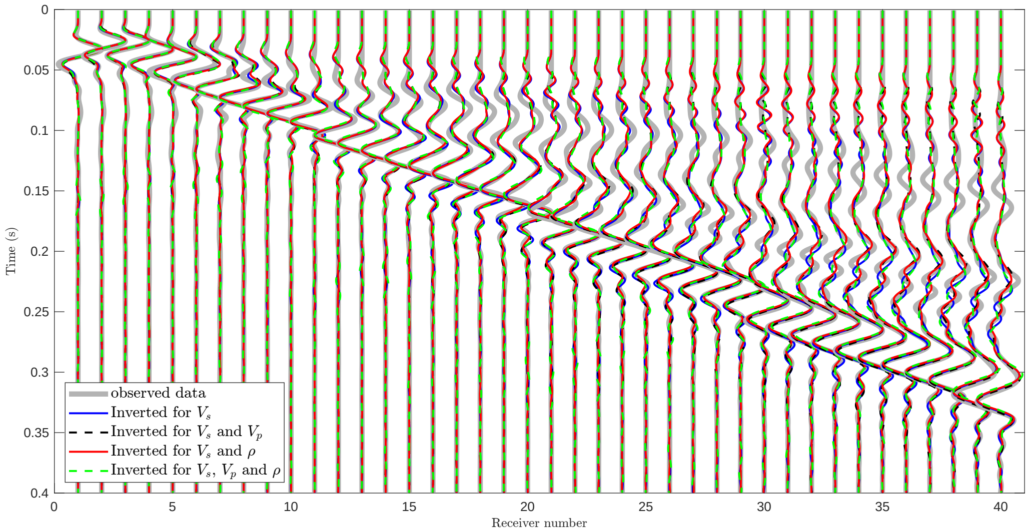

Figure 5.2: *Observed (gray) and synthetic (colored) vertical-component seismograms for the synthetic test. Blue seismograms: V_s-only; black: V_s and V_p; red: V_s and ρ; green: V_s, V_p and ρ.*

5.5 2D inversion results

The inverted 2D V_s models are broadly consistent across all parameterizations.

- In the V_s-only and V_s–V_p inversions, the recovered structures are nearly identical, resolving the shallow low-velocity zone (LVZ) and the increase in velocity with depth.
- When ρ is included (either in V_s–ρ or V_s–V_p–ρ), the V_s field changes more noticeably: between about 5–15 m depth, velocities become higher than in the V_s-only or V_s–V_p cases. This illustrates a parameter trade-off, where part of the waveform sensitivity is absorbed into ρ, which in turn modifies the V_s field.
- The V_p models remain close to the starting values, with only minor variations, confirming the weak sensitivity of Rayleigh waves to compressional velocity 5.3.

5.6 Discussion

The synthetic test provides three key insights:

1. **V_s is reliably constrained.** Across all parameterizations, V_s recovered in a stable and interpretable manner.
2. **ρ and V_p are not robustly recovered.** Density updates in particular are a bit far from the true model, even though they improve the V_s recovery and lower the misfit.

V_p shows minor changes and remain close to the starting values.

3.

In practical terms, the test confirms that Rayleigh waves alone constrain V_s robustly but cannot resolve ρ or V_p without ambiguity. For the field data, this means that V_s can be interpreted with confidence, but any structure in V_p or ρ should be treated with caution unless complemented by additional wave types.

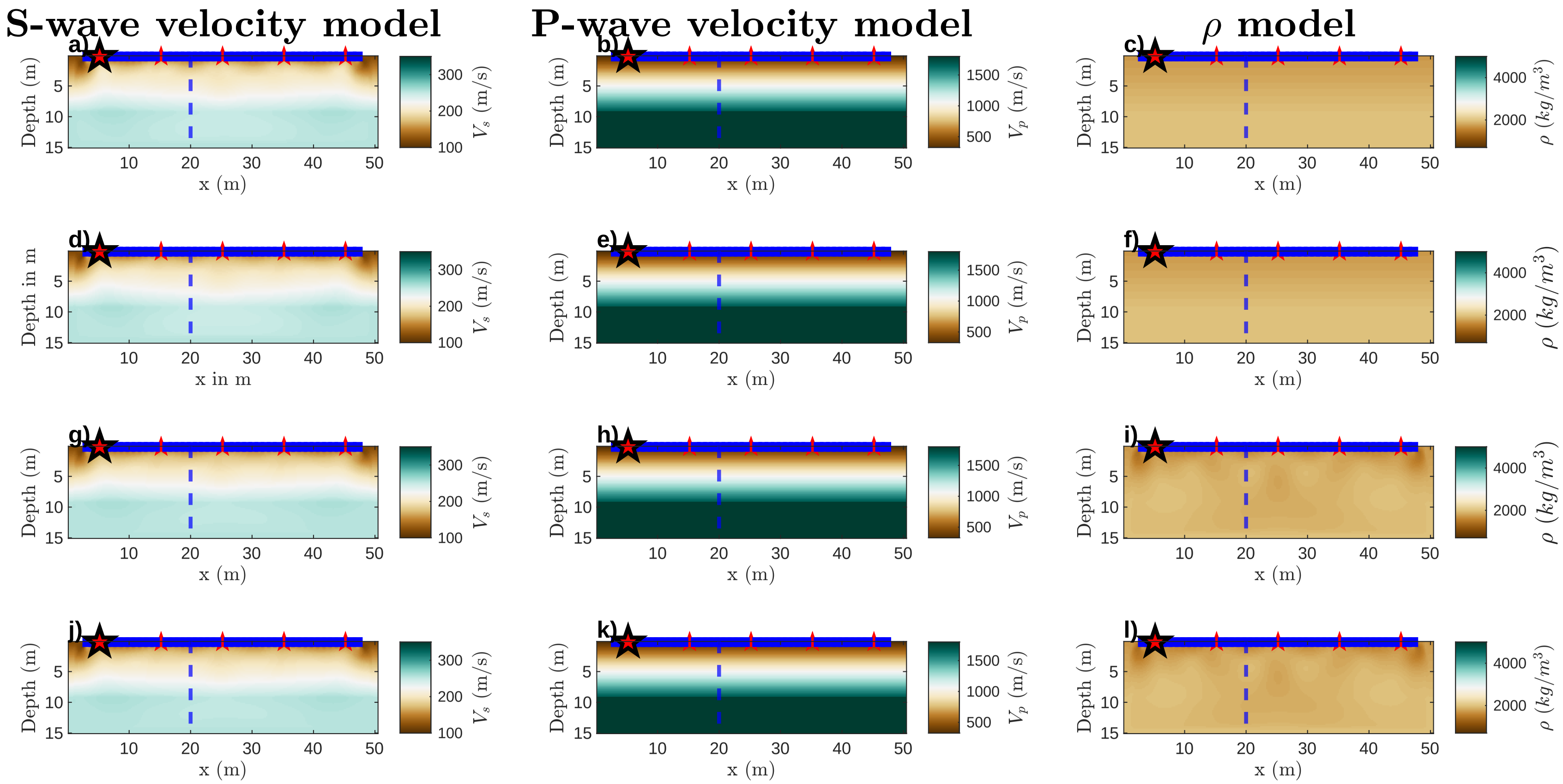

Figure 5.3: *Final 2D inversion results for the synthetic test under different parameterizations. Panels (a–c) show the* V_s, V_p, *and* ρ *models for the* V_s–V_p *inversion; (d–f) the corresponding models for* V_s–ρ; *(g–i) for* V_s–V_p–ρ; *and (j–l) for the* V_s*-only reference. The* V_s *models are consistent across all cases, with higher velocities between 5–15 m depth once* ρ *is included, indicating parameter trade-offs. The* V_p *models remain close to the starting models with only minor adjustments, while the* ρ *models show weak and non-robust updates.*

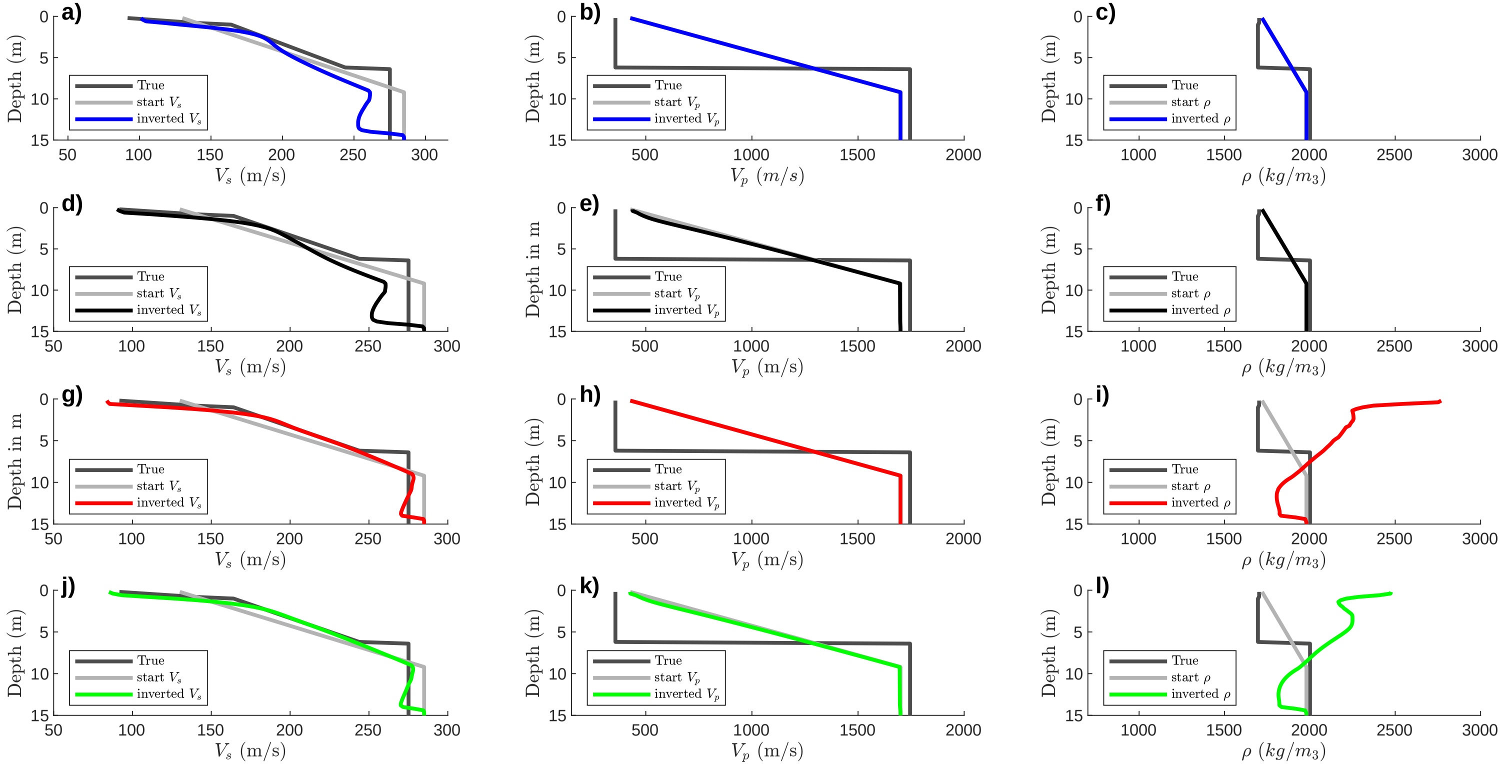

Figure 5.4: *1D 1D depth profiles from the synthetic test were extracted at a 20 m offset (dashed blue line in Fig. 5.3). The recovery of V_s improves when density is included in the inversion(V_s and ρ, V_s, V_p and ρ). In contrast, the ρ profiles remain far from the true model, while V_p shows only a slight variation in the uppermost meter and otherwise remains identical to the starting model.*

Chapter 6

Results

This chapter presents the results of the elastic full-waveform inversion (FWI) applied to the two perpendicular seismic profiles acquired at the Herrenknecht test site, which are referred to as Profile A and Profile B. The analysis is structured to address the main objectives of this thesis in a systematic way. The first step focuses on the inversion of shear-wave velocity (V_s) only. Since Rayleigh waves are most sensitive to V_s, with weaker sensitivity to compressional velocity (V_p) and density (ρ), inverting V_s alone provides the most stable and reliable baseline model. This baseline serves as a reference for later comparisons. In the next step, the inversion is extended to multiple parameters. Different combinations of V_s, V_p, and ρ are updated jointly in order to evaluate the potential benefits and limitations of multi-parameter inversion in the near-surface context. This comparison with the V_s-only baseline highlights possible trade-offs between parameters and tests whether additional model updates significantly improve the fit to the data. The third part investigates the sensitivity of the inversion to the starting model. Since FWI is a local optimization method, the recovered model may depend on the chosen starting model. To examine this effect, an alternative starting model is introduced and the results are compared against the baseline inversions. Finally, the two profiles are cross-validated at their intersection point. Because Profiles A and B were inverted independently, agreement of the recovered velocity structures at their crossing serves as an internal consistency check and increases confidence in the robustness of the methodology. Each of these steps is presented separately for Profiles A and B to allow a clear and consistent interpretation of the results.

6.1 Single-parameter inversion: V_s only

The case where only the shear-wave velocity (V_s) is inverted, while compressional velocity (V_p) and density (ρ) are kept constant at 1440 m/s and 1880 kg/m^3, respectively. This configuration provides a stable baseline because Rayleigh waves are predominantly sensitive to V_s, whereas their sensitivity to V_p and ρ is comparatively weak. The starting V_s model was derived from dispersion-curve inversion and extended to two dimensions to match the acquisition geometry. Figures 6.1 and 6.5 show the initial and final V_s models for Profiles A and B, respectively.

6.1.1 Profile A

To evaluate the inversion result, Figure 6.2 compares the V_s depth profile at distance of 20 meters in Profile A. The gray line represents the dispersion-derived starting model, while the blue line shows the FWI result after 80 iterations. The starting model exhibits the four-layer parameterization imposed by the dispersion-curve inversion, with sharp velocity steps at the layer boundaries. By contrast, the inverted profile resolves a smoother and more continuous velocity increase with depth, although some sharp contrasts and layering remain after 80 iterations. The near-surface low-velocity layer (~200 m/s in the top 3–5 m) is clearly recovered, followed by a sharp increase to 350–600 m/s at 17 depth. This comparison illustrates two key points: (i) the FWI result preserves the main features of the starting model, and (ii) the inversion suppresses the artificial layering of the initial model, yielding a geologically plausible trend consistent with expectations for the gravel-rich subsurface at the site.

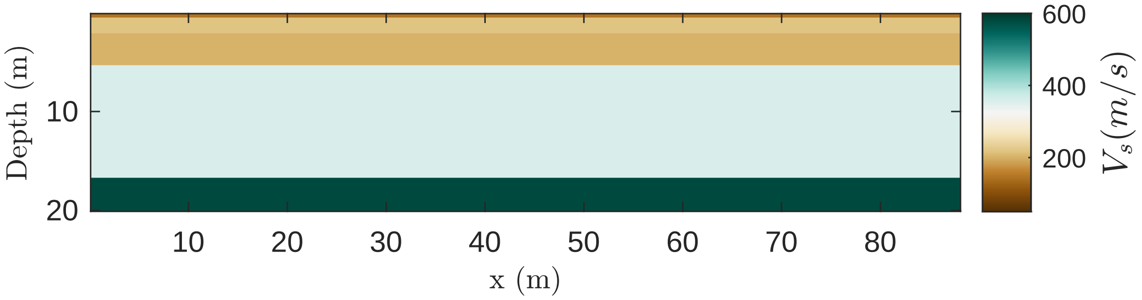

(a) *four layer V_s starting model*

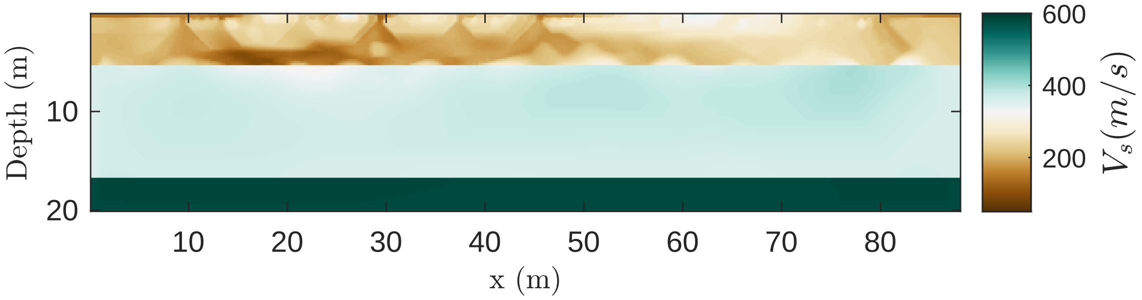

(b) *final V_s model after 80 iterations*

Figure 6.1: *Starting and final models for Profile A in the V_s-only inversion. Panel (a) show the initial parameterization: a four-layer V_s model derived from dispersion-curve analysis. Panel (b) displays the corresponding final model after 80 iterations of FWI.*

The inversion performance is evaluated using the evolution of the misfit function. Figure 6.3 shows the normalized misfit as a function of iteration number for Profile A. The dashed black lines mark the frequency stages of the multi-scale strategy (see Chapter 2). Each stage begins with a temporary increase in misfit as new frequency content is introduced, followed by a steady decrease as the model adapts. After 80 iterations at stage 6, we have the lowest misfit by adding high frequency.Thus, we can see the misfit is increasing, which is also normal, as that inversion normally works best in low frequencies and becomes problematic in high frequencies.

Across all stages, the misfit shows a consistent downward trend, indicating progressive model improvement and a stable inversion process. The misfit decreases from 1.7 to 1.1, demonstrating substantial improvement in the agreement between observed and synthetic seismograms. This behavior is typical for multi-scale FWI and indicates that the inversion converged in a controlled manner rather than becoming trapped in local minima.

Finally, the quality of the inversion result can be assessed directly by comparing observed and synthetic seismograms. Figure 6.4 shows vertical-component recordings for Profile A, with observed data in gray and synthetics generated from the inverted V_s model after 80 iterations in blue. The agreement between the two datasets is good across the full receiver spread. Both the dispersive character and the overall amplitude decay of the

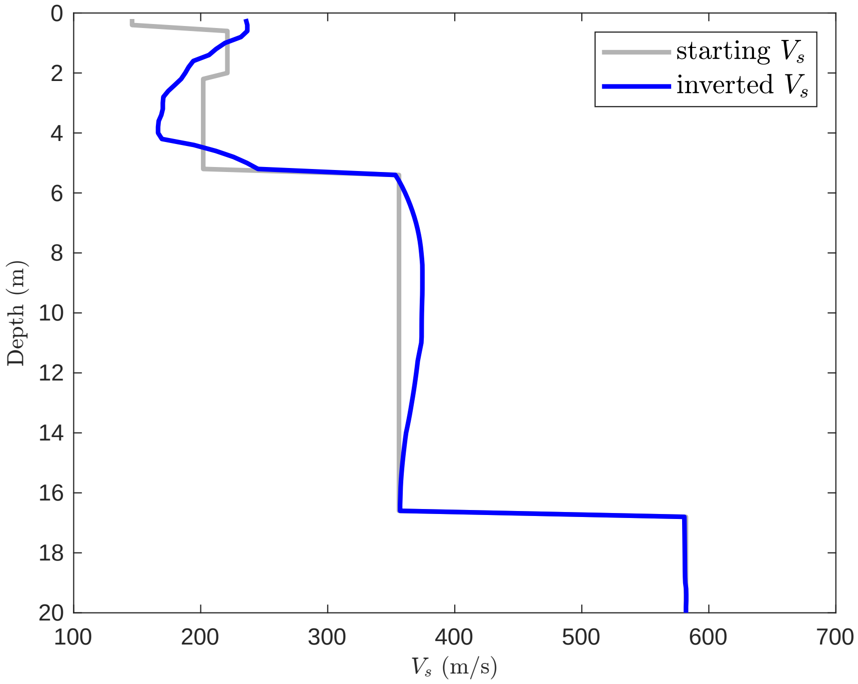

Figure 6.2: *Comparison of starting and inverted V_s depth profiles at distance of 20 m of Profile A. The inversion resolves a low-velocity layer of about 200 m/s in the top 3–5 m, underlain by a sharp increase to 350–600 m/s.*

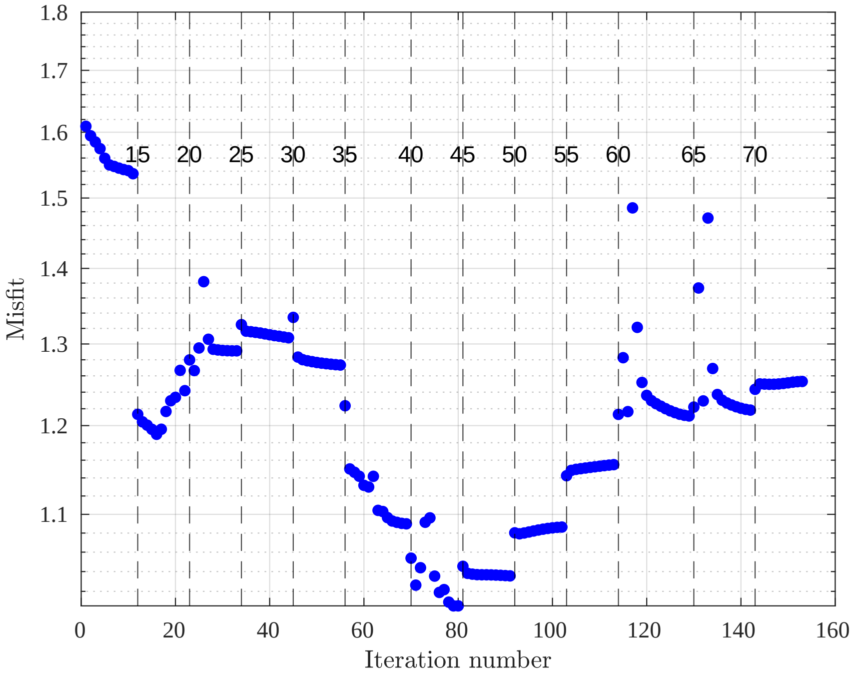

Figure 6.3: *Evolution of the misfit during V_S-only inversion for Profile A. Dashed black lines indicate the frequency stages of the multi-scale strategy. Each stage begins with a temporary increase in misfit as higher frequency content is introduced, followed by a steady decrease as the model adapts. Overall, the misfit decreases from ∼1.7 to ∼1.1, demonstrating stable convergence and effective use of the frequency continuation approach.*

Rayleigh wave-train are well reproduced. Minor differences remain in the early arrivals and in some of the later coda energy, which may reflect limitations of the two-dimensional modeling or unmodeled small-scale heterogeneity. Importantly, however, the fundamental dispersion trend is matched, indicating that the inverted V_s model captures the dominant structural features of the shallow subsurface. This data-fit comparison provides an essential validation: while the misfit curve (Figure 6.3) demonstrates numerical convergence, the seismogram overlay confirms that the recovered model reproduces the observations in physically meaningful terms. Together, these results show that the V_s-only inversion for Profile A yields a robust and geologically plausible model.

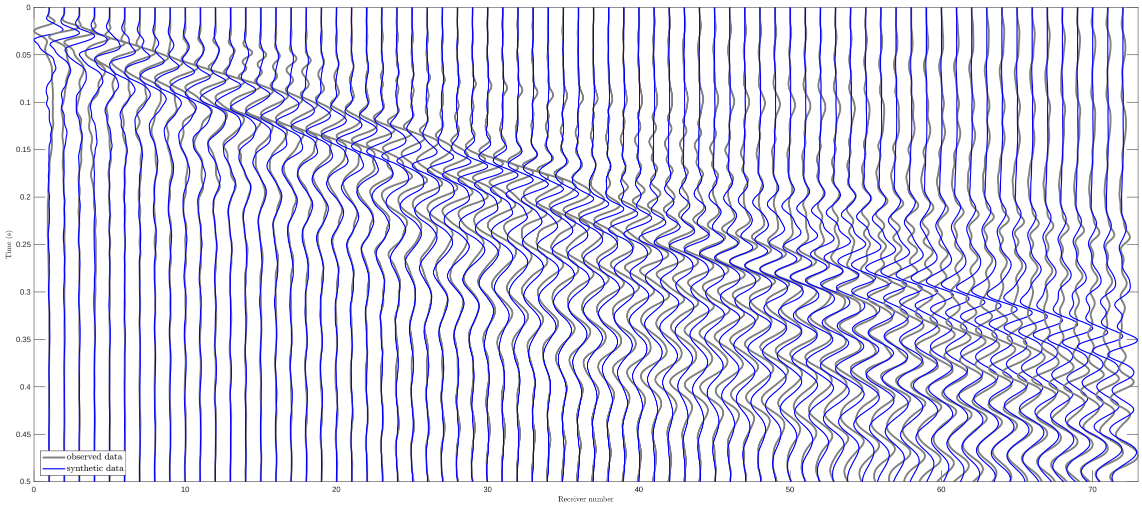

Figure 6.4: *Comparison of observed and synthetic vertical-component seismograms for the first shot of Profile A after V_s-only inversion is shown. The gray traces are observed data, and the blue ones are synthetic traces after 80 iterations. The good agreement across the receiver spread, particularly in the dispersive Rayleigh wavetrain, confirms that the recovered V_s model provides an adequate explanation of the recorded data. Residual differences at large offsets are attributed to noise and unmodeled small-scale heterogeneity.*

6.1.2 Profile B

For Profile B, the V_s-only inversion was performed in the same way as for Profile A. The starting shear-wave velocity model was derived from dispersion-curve inversion and laterally extended to match the survey geometry. As before, the compressional velocity and density were fixed at constant values of 1440 m/s and 1880 kg/m^3, respectively. Figure 6.5 compares the initial and inverted model. The starting V_s model is characterized by the layered structure typical of dispersion inversions, with distinct step-like contrasts at the imposed boundaries and no lateral variability. After 60 iterations, the inversion produces a smoother structure: a near-surface low-velocity layer of about 200 m/s in the upper 3–5 m is recovered, underlain by a sharp rise to 200–350 m/s and a another sharp increase to 350–650 m/s at depth. These values are consistent with the gravel-rich deposits at the test site, but in Profile B the transition to higher velocities occurs slightly deeper than in Profile A, suggesting subtle lateral variability. The depth profile confirms this refinement: while the inverted curve retains the overall structure of the starting model, it smooths the unrealistic step changes in the upper few meters and yields a more geologically plausible velocity trend.

The inversion performance for Profile B is illustrated by the misfit evolution in Figure 6.7. The misfit decreases from 1.6 at the start to the lowest amount 1.1 after 60 iterations. As in Profile A, each frequency stage begins with a slight misfit increase due to the introduction of

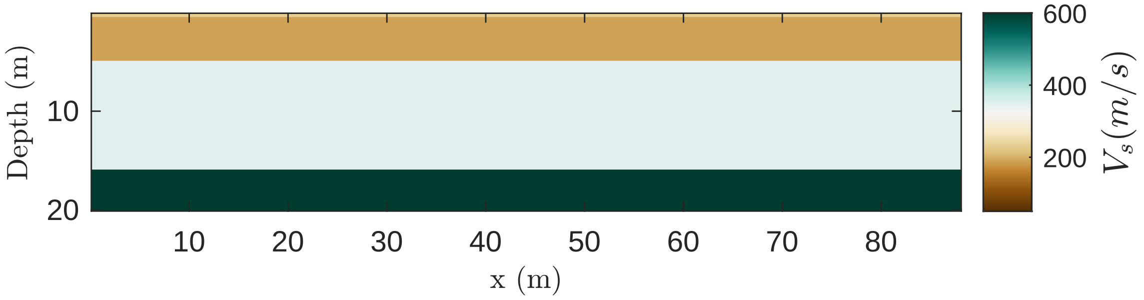

(a) *four layer V_s starting model*

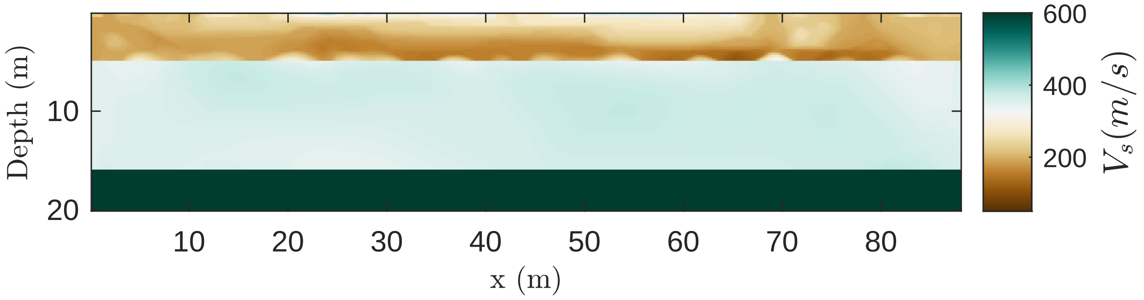

(b) *final V_s model after 80 iterations*

Figure 6.5: *Starting and final model for Profile B in the V_s-only inversion. Panel (a) shows the initial parameterization: a four-layer V_s model derived from dispersion-curve analysis. Panel (b) displays the corresponding final model after 60 iterations of FWI.*

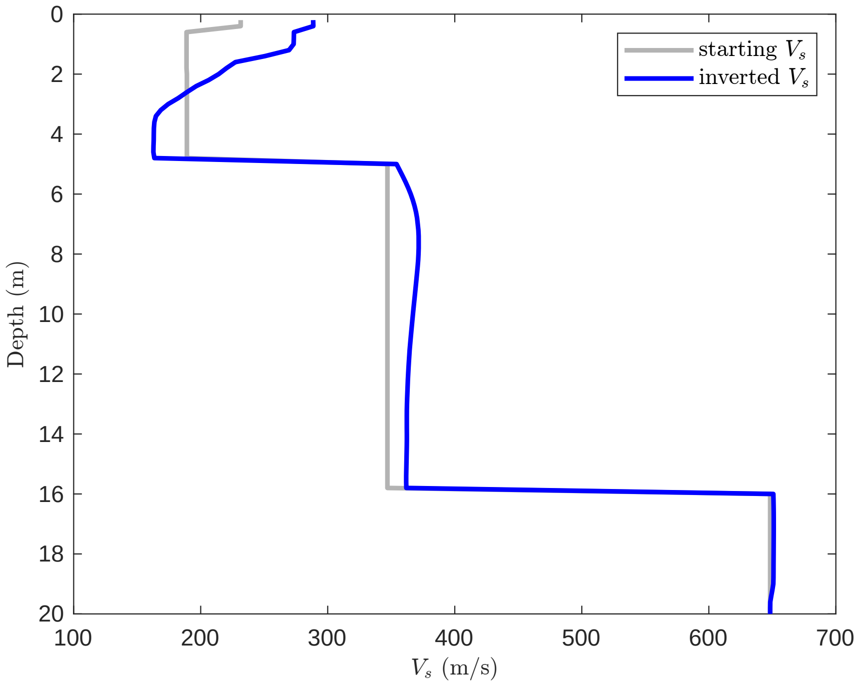

Figure 6.6: *Comparison of starting and inverted V_s depth profiles at 20 m offset for Profile B. The starting model (gray) shows the four-layer parameterization from dispersion inversion, while the inverted profile (blue) resolves a smoother trend. A low-velocity layer of about 200 m/s in the upper 3–5 m is recovered, followed by a sharp increase to 200–350 m/s and a gradual rise toward 350–650 m/s.*

higher-frequency content not yet captured by the model, followed by a steady reduction as the inversion adapts. This staged convergence is characteristic of stable FWI and confirms that the inversion avoided local minima. The inversion is validated by direct comparison between observed and synthetic seismograms (Figure 6.8). The synthetic traces generated from the final V_s model reproduce the dispersion trend and amplitude decay of the Rayleigh wave-train with good accuracy across the receiver spread. Some mismatches remain in the later arrivals and at large offsets, similar to Profile A. These discrepancies likely reflect a combination of field noise and fine-scale heterogeneity not captured by the two-dimensional model. Nevertheless, the fundamental dispersion behavior is well matched, confirming that the inverted model captures the dominant features of the shallow subsurface.

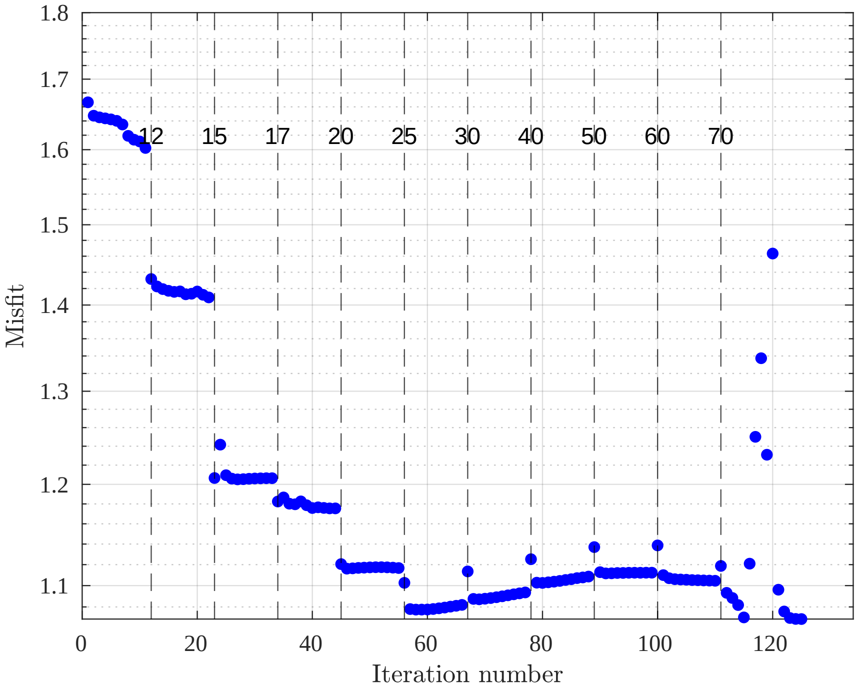

Figure 6.7: *Evolution of the misfit during V_s-only inversion for Profile B. Dashed gray lines indicate the frequency stages of the multi-scale strategy. Each stage shows an initial rise in misfit as higher frequency content is introduced, followed by a steady decrease as the model adapts. Overall, the misfit decreases from ∼1.6 to ∼1.1, confirming stable convergence and effective use of the frequency continuation approach.*

Overall, the V_s-only inversion for Profile B provides a consistent and geologically reasonable velocity structure that closely agrees with the results from Profile A. The agreement between the two independently inverted profiles increases confidence in the robustness of the methodology and establishes a reliable baseline for the subsequent multi-parameter inversions and sensitivity analyses.

Summary of V_s-only inversion

The V_s-only inversions for Profiles A and B yield consistent and geologically credible velocity structures. In both cases, the dispersion-derived four-layer starting model is refined into a smoother trend while preserving the key velocity contrasts. A low-velocity layer of about 200 m/s in the upper 3–5 m is clearly resolved, underlain by a sharp increase to 200–350 m/s and a rise toward 600–700 m/s at greater depths. These refinements are accompanied by stable convergence under the multi-scale frequency strategy, and the comparisons of observed–synthetic data confirm that the inverted models reproduce the

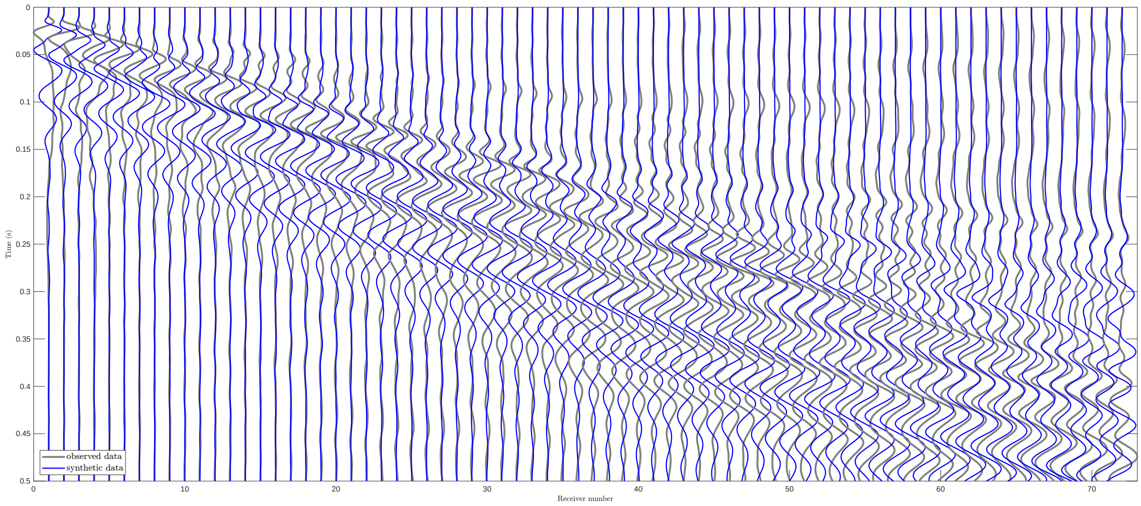

Figure 6.8: *Comparison of observed (gray) and synthetic (blue) vertical-component seismograms for Profile B after 60 iterations of V_s-only inversion. The synthetic data reproduce the dispersive Rayleigh-wave train and amplitude decay with good accuracy across the receiver spread. Residual differences in later arrivals and at larger offsets are attributed to noise and small-scale heterogeneity not represented in the 2D model.*

dispersive Rayleigh wavefield with good accuracy. Taken together, the results establish a robust baseline for the subsequent multi-parameter inversions and sensitivity tests.

6.2 Multi-parameter inversion

The previous section demonstrated that inverting only for V_s provides a robust and geologically plausible baseline model. This is expected, since Rayleigh waves are predominantly sensitive to shear-wave velocity. However, the ultimate aim of this study is not only to recover V_s, but to evaluate whether a more complete near-surface model — including V_p and ρ — can also be reconstructed from the available data. A reliable elastic reference model is essential for the UVT project, where it will be used both to validate the vibroseis source signature and to invert for the source force. The key question is therefore: can reliably recover all three parameters (V_s, V_p, and ρ) in FWI, from Rayleigh-wave dominated data, and what do we gain if include V_p or ρ in addition to V_s? This section is designed to address that question directly. Testing different parameterizations is essential: first, to see whether including additional parameters improves the data fit, especially amplitude reproduction; and second, to assess which model components are robust and which remain poorly constrained. To explore these issues, four parameterizations are tested systematically: (i) V_s only, (ii) V_s and ρ, (iii) V_s and V_p, and (iv) V_s, V_p and ρ. The V_s-only case serves as the reference against which all others are compared. For each profile, present (a) 2D starting and final models, (b) depth profiles extracted at the profile midpoint (at distance of 44 m), (c) misfit evolution, and (d) observed–synthetic data fits. This consistent structure allows us to assess, step by step, how the choice of parameterization influences the inversion results for both Profiles A and B.

6.2.1 Profile A

For Profile A, the same four-layer V_s starting model as in the V_s-only case was used (Figure 6.1a). Compressional velocity and density were kept at homogeneous background values of 1440 m/s and 1880 kg/m^3, respectively. In the multi-parameter inversions, V_p and/or ρ were allowed to vary with V_s, depending on the chosen parameterization. The workflow itself was identical to the V_s-only case, ensuring that any differences reflect parameterization rather than setup. Results are presented in the same sequence as before: (a) final 2D models for each parameterization, (b) depth profiles at the distance of 20 m, (c) misfit evolution, and (d) comparison of observed–synthetic. Figure 6.9 shows the 2D models. Across all cases, the main V_s structure remains consistent with the V_s-only inversion: a shallow low-velocity layer overlying higher velocities at depth. However, localized anomalies (e.g., a 300 m/s low-velocity patch near 25 m , 10 m depth, and a higher-velocity zone at 75 m) appear in the V_s and V_s–V_p cases but disappear once ρ is included. This indicates parameter trade-offs: when ρ is allowed to vary, some waveform informations are into density, suppressing spurious velocity contrasts in V_s. The V_p models highlight the weak sensitivity of Rayleigh waves to compressional velocity. In the V_s and V_p case, the inversion produces a central high-velocity block and two shallow low-velocity zones ($\sim$1000 m/s). These disappear in the V_s, V_p and ρ case, again reflecting cross-talk between V_p and ρ. The ρ models themselves remain close to the homogeneous starting model in both V_s–ρ and V_s–V_p–ρ inversions, with only minor, non-systematic fluctuations. This confirms that density is effectively unconstrained by Rayleigh-wave data, consistent with theoretical sensitivity expectations. Depth profiles at 20 m (Figure 6.10) confirm that V_s recovery is robust across all parameterizations, while V_p and ρ curves remain close to their starting values with only small, non-systematic deviations. In summary, the results for Profile A highlight two main points: (i) V_s inversion is stable and consistent, regardless of parameterization; and (ii) V_p and ρ cannot be reliably recovered from Rayleigh-wave-dominated data alone, as their updates are unstable or dominated by trade-offs. This underlines the need for complementary body-wave or multi-component data to achieve a fully constrained elastic model.

An important measure of inversion performance is the behavior of the objective function over the iterations. Figure 6.11 shows the misfit for the four parameterizations tested on Profile A. The V_s-only inversion provides the most stable convergence, with a steady decrease over 140 iterations. Adding V_p (V_s–V_p inversion) produces a similar curve, and all parameterizations show stable convergence after about 80 iterations. Notably, the misfit curves for V_s–V_p and V_s–V_p–ρ overlap almost completely, making them indistinguishable on the basis of misfit alone. The full three-parameter inversion (V_s–V_p–ρ) does not achieve further reduction compared to the V_s–ρ case. Instead, its curve remains at an intermediate level, suggesting that the additional V_p updates are not supported by the data and may even hinder convergence. This agrees with the 2D and 1D model results, where spurious V_p anomalies disappeared once ρ was included. Overall, these results highlight that misfit reduction is not sufficient to judge the quality of a multi-parameter inversion. Different parameterizations can yield very similar misfit values while producing substantially different models. Therefore, the misfit curves must be interpreted in conjunction with the recovered 2D models and depth profiles to assess whether the updates provide meaningful constraints on V_p or ρ.

To assess whether including additional parameters improves the models, the data fit must be examined directly. Figure 6.12 compares observed and synthetic seismograms for the four parameterizations for the shot at the middle of the profile shot. The observed data are shown in gray, while synthetics from the inverted models are displayed in blue (V_s only), black (V_s and V_p), red (V_s and ρ), and green (V_s, V_p and ρ). All four inversions reproduce the dispersive Rayleigh wave-train with reasonable accuracy, confirming that the V_s field is robustly constrained in every case. Minor amplitude and phase differences remain, but no systematic improvement results from including V_p or ρ. Taken together with the misfit evolution, these comparisons demonstrate a central point: while multi-parameter inversions achieve numerical convergence similar to the V_s-only case, they do not add

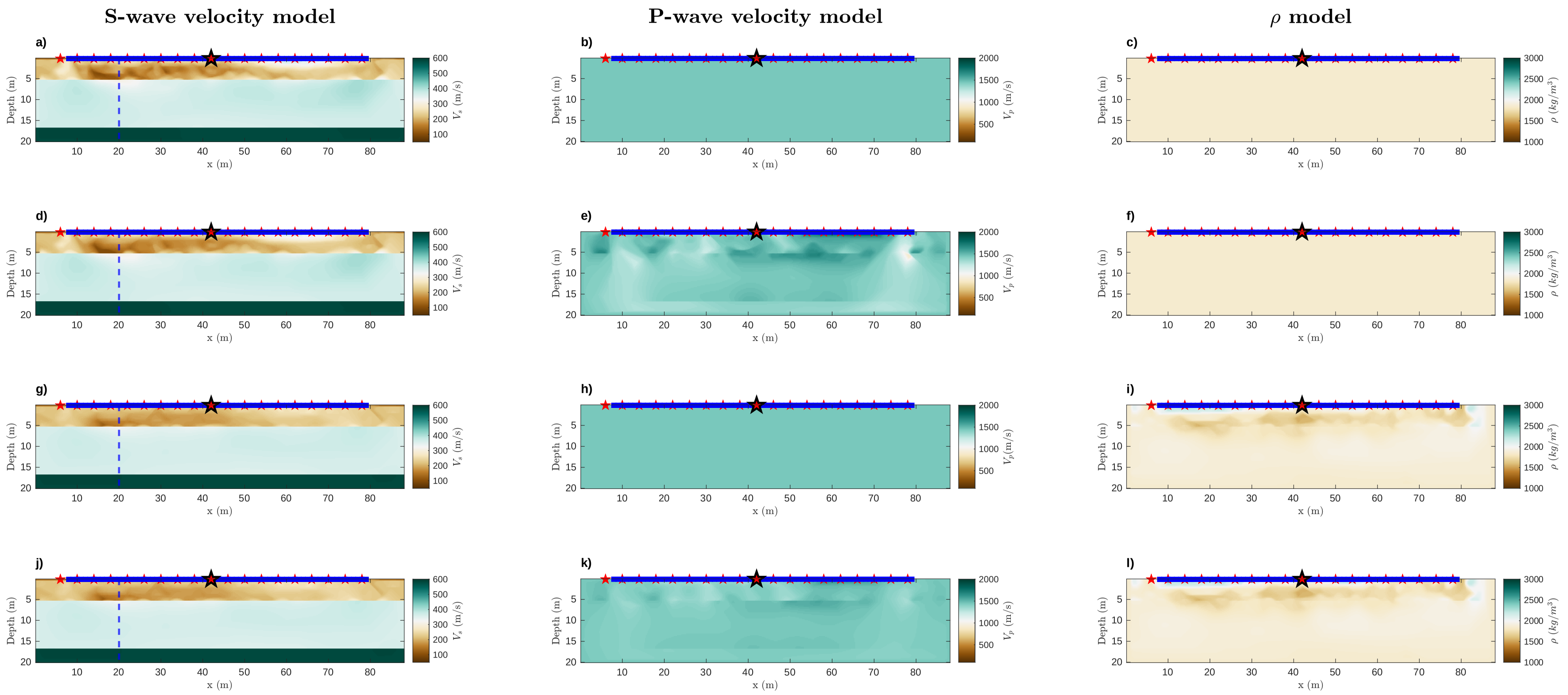

Figure 6.9: *Comparison of final 2D inversion results for Profile A under different parameterizations. Panels (a–c) show the V_s, V_p, and ρ models for the V_s and V_p inversion; (d–f) the corresponding models for V_s and ρ; (g–i) for V_s, V_p and ρ; and (j–l) for the V_s-only reference. The dashed blue lines indicate the location of the vertical profiles shown in Figure 6.10 While the V_s structures are broadly similar across all tests, distinct differences emerge in localized features, particularly in the 5–15 m depth range. Inversions involving V_p introduce high- and low-velocity anomalies that vanish once ρ is included, highlighting parameter trade-offs. The ρ models remain nearly homogeneous across multi-parameter tests, underlining the weak sensitivity of Rayleigh waves to density.*

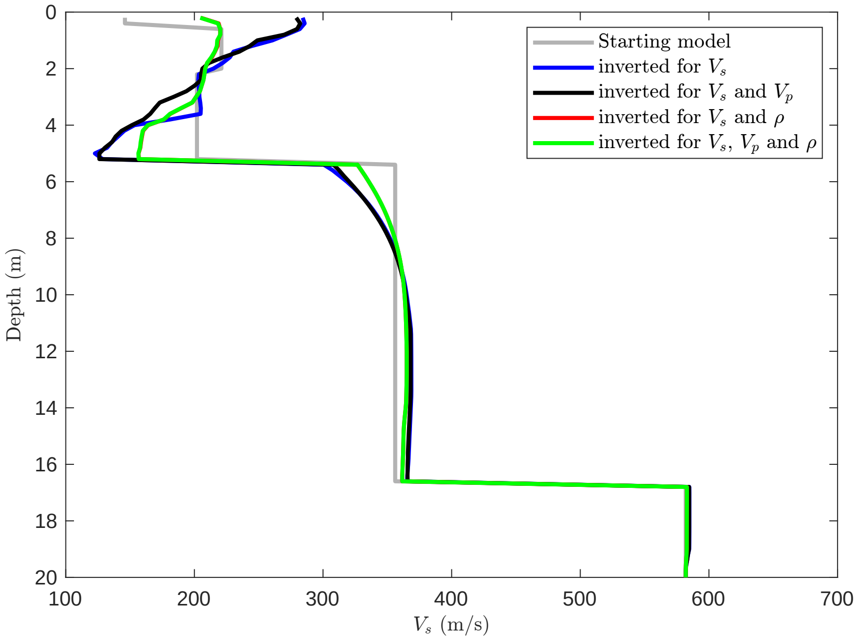

Figure 6.10: *Depth profiles of shear-wave velocity at the distance of 20 m of Profile A comparing starting (gray solid line) and inverted (solid colored) for different parameterizations. Panels (a–c) show V_s, V_p, and ρ for the V_s–V_p inversion; (d–f) for V_s–ρ; (g–i) for V_s–V_p–ρ; and (j–l) for the V_s-only case. In all cases, the near-surface low-velocity zone ($V_s \approx 200$ m/s) is recovered, underlain by a sharp increase to 350–600 m/s. V_p updates show localized anomalies (e.g., a block of elevated velocity at 10–17 m depth) that are suppressed when ρ is included.*

reliable structural information when constrained by Rayleigh waves alone. The V_s model remains the dominant and trustworthy outcome, whereas the V_p and ρ fields are poorly constrained and prone to trade-offs.

6.2.2 Profile B

For Profile B, the multi-parameter inversions were performed using the dispersion-derived V_s starting model introduced in Section 6.1, together with homogeneous background values of $V_p = 1440$ m/s and $\rho = 1880$ kg/m^3. As in Profile A, tested three joint parameterizations (V_s and V_p, V_s and ρ, V_s, V_p and ρ) in addition to the V_s-only reference. The inversion workflow and multi-scale strategy remain unchanged. To avoid repeating the detailed procedure already described for Profile A, the focus here is on the outcomes. We present the results in the same order: 2D models, depth profiles at the 20 m distance, misfit evolution, and data–fit plots—emphasizing how the findings from Profile B confirm or differ from those of Profile A. This provides a direct test of the repeatability and robustness of the inversion strategy across two independent profiles. The 2D inversion results for Profile B (Figure 6.13) show that the recovered V_s field is laterally more homogeneous than for Profile A. In both the single- and multi-parameter cases, V_s varies primarily with depth, and fewer localized anomalies are present. This difference is consistent with the raw field data, where Profile A displayed stronger lateral variability in the Rayleigh wavetrain. The near-surface low-velocity layer (~200 m/s in the top 3–5 m) and the subsequent increase to 600–700 m/s at depth are again robustly recovered across all parameterizations. The V_p models from the V_s–V_p and V_s–V_p–ρ inversions display three high-velocity blocks in the central part of the model, flanked by shallow low-velocity zones near of 20 m and 60–80 m. These patterns mirror those in Profile A but are more pronounced here. Their disappearance

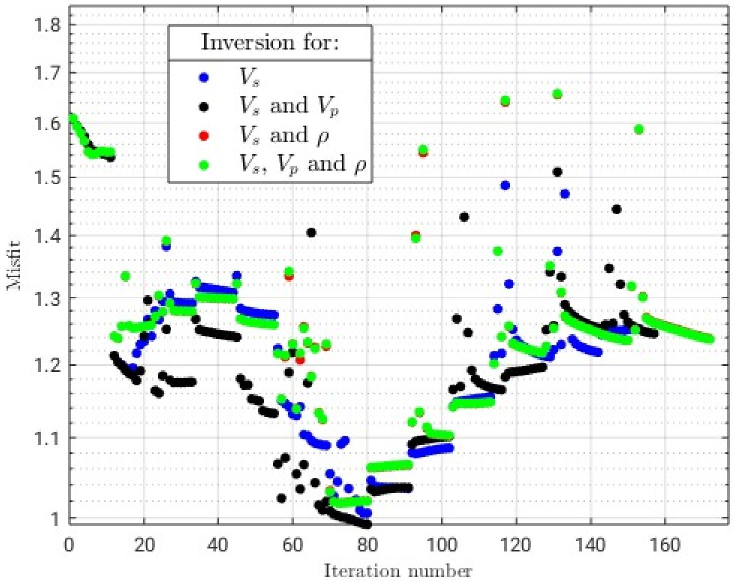

Figure 6.11: *Evolution of the misfit during Profile A inversions for the four parameterizations. The* V_s*-only inversion shows the most stable convergence, with a steady decrease across the frequency stages. The* V_s–V_p *and* V_s*,* V_p *and* ρ *curves overlap closely, reflecting the weak sensitivity of Rayleigh waves to* V_p *and the trade-offs introduced when multiple parameters are inverted simultaneously. The* V_s *and* ρ *inversion achieves a comparable reduction but does not provide additional stability. Overall, the misfit behavior confirms that* V_s *dominates the inversion, whereas* ρ *exerts only a secondary influence and* V_p *remains essentially unconstrained.*

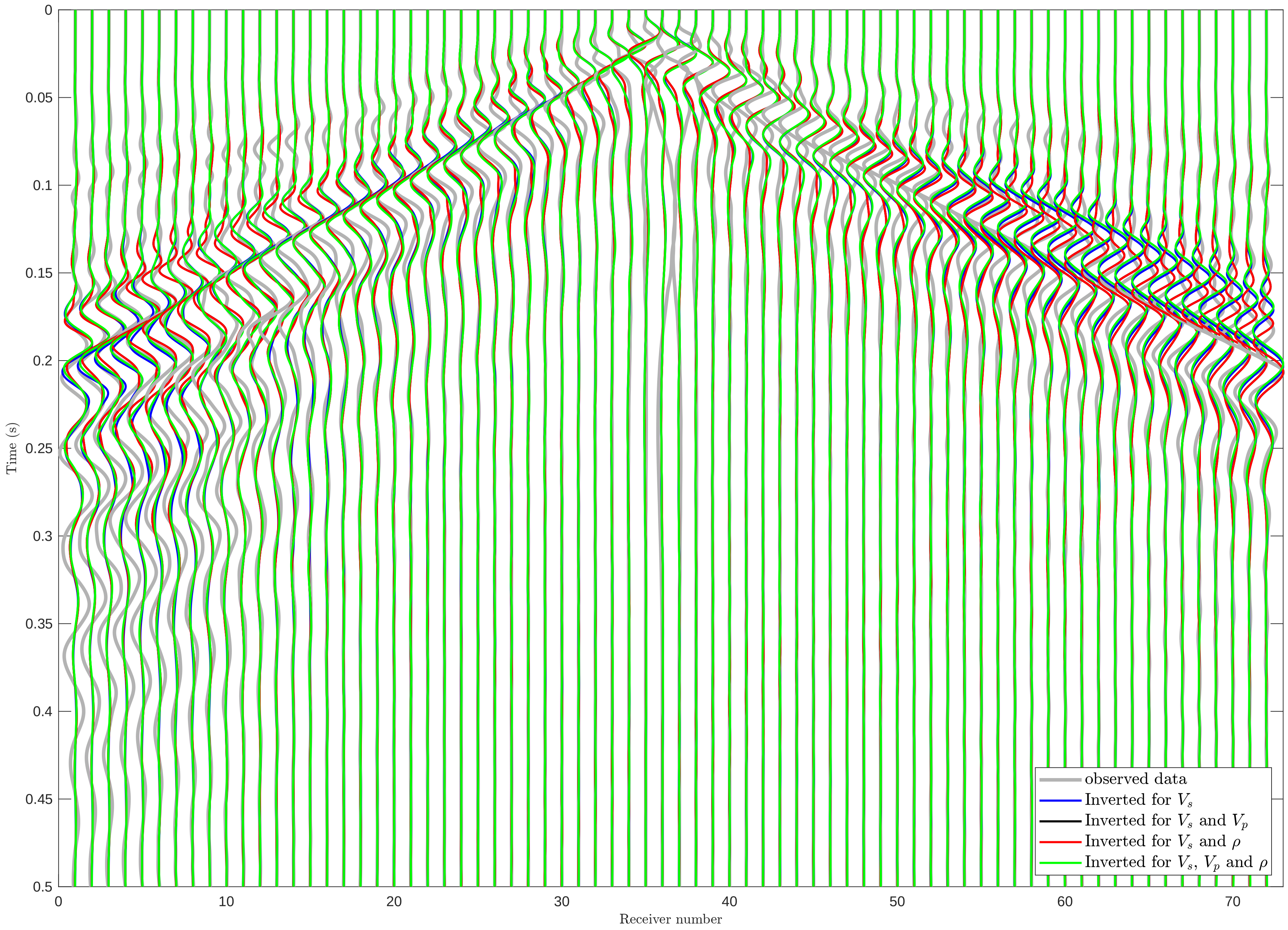

Figure 6.12: *Observed (gray) and synthetic (colored) vertical-component seismograms for Profile A after 140 iterations. Blue lines correspond to the V_s-only inversion, black to V_s and V_p, red to V_s and ρ, and green to V_s, V_p and ρ. All parameterizations reproduce the dispersive Rayleigh wavetrain and overall amplitude decay with good accuracy. Minor differences exist in amplitude matching, but no systematic improvement is observed when V_p or ρ are included. The consistency across parameterizations demonstrates that V_s is robustly constrained, while V_p and ρ remain poorly resolved.*

once ρ is included again indicates parameter trade-offs: the inversion can explain part of the waveform mismatch equally well by updating ρ, which reduces instability in V_p. The ρ models remain close to the homogeneous background in both V_s–ρ and V_s–V_p–ρ inversions, with only minor, non-systematic deviations. This confirms once more that density is not constrained by Rayleigh waves in this setup. Depth profiles (Figure 6.14) confirm these observations. The V_s profiles are nearly identical across all parameterizations, consistently resolving the low-velocity near-surface layer followed by a sharp increase with depth. The V_p profiles show localized in the V_s–V_p case, but these vanish once ρ is included, reinforcing the interpretation that such anomalies are not robust. As in Profile A, ρ remains essentially unaltered. Together, the 2D and 1D results demonstrate that Profile B supports the same main conclusions as Profile A: V_s can be recovered reliably, V_p updates are unstable and strongly affected by trade-offs, and ρ cannot be constrained from Rayleigh waves alone. The greater lateral homogeneity in Profile B further highlights that differences between the two profiles are geological in origin, consistent with the raw field data.

The misfit evolution for Profile B (Figure 6.15) differs from that of Profile A. All four parameterizations show a steady overall reduction in misfit, but the curves are more clearly separated here. The V_s-only inversion converges most smoothly, with a monotonic decrease across the frequency stages. When V_p is included (V_s–V_p), the misfit remains consistently higher, reflecting the weak sensitivity of Rayleigh waves to compressional velocity and the instability introduced by the extra degree of freedom. The V_s–ρ inversion achieves the lowest misfit, but with stronger oscillations, reflecting the amplitude sensitivity of Rayleigh waves to density. The full three-parameter inversion (V_s–V_p–ρ) again tracks closely with the V_s–V_p case, confirming that V_p updates are not supported by the data and that adding ρ does not lead to a stable improvement. The misfit curves therefore suggest that including ρ can lower the objective function, whereas V_p contributes little. However, misfit reduction is not a reliable indicator of model quality. The observed–synthetic data comparison (Figure 6.16) puts these results into perspective. All four parameterizations reproduce the dispersive character of the Rayleigh wavetrain and the overall amplitude decay across the receiver line. Minor amplitude mismatches remain, but there is no systematic improvement when V_p or ρ are included in addition to V_s. In fact, the synthetics from the V_s-only and V_s–ρ inversions match the observed data as well as, or better than, the more complex parameterizations. Overall, Profile B confirms that V_s is the only parameter robustly constrained by the Rayleigh-wave data. Density can influence the misfit through amplitude adjustments, but the resulting updates are unstable and not geologically meaningful, while compressional velocity remains essentially unconstrained. Profile B therefore reinforces the robustness of the V_s recovery and underscores the limited value of multi-parameter FWI in Rayleigh-wave-dominated data.

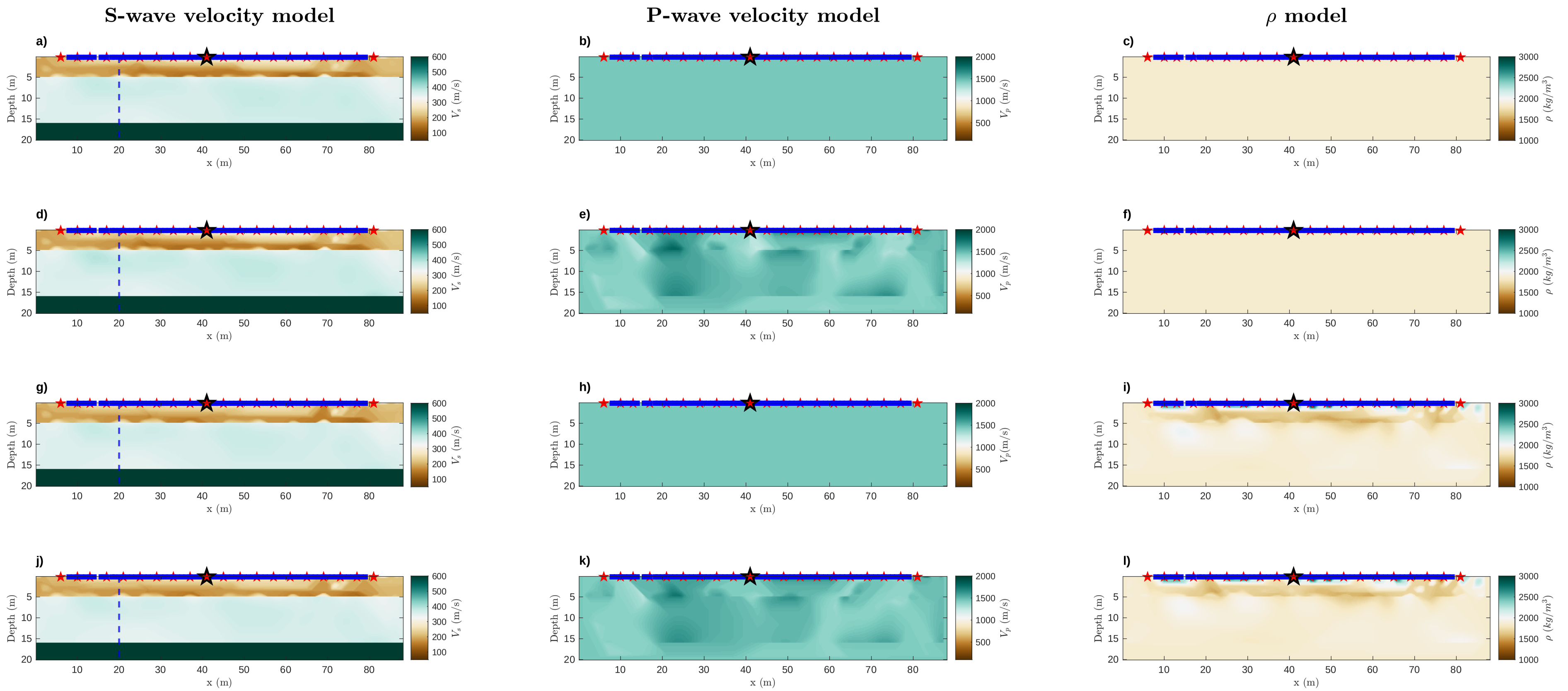

Figure 6.13: *Final 2D inversion results for Profile B under different parameterizations. Panels (a–c) show the V_s, V_p, and ρ models for the V_s–V_p inversion; (d–f) the corresponding models for V_s–ρ; (g–i) for V_s–V_p–ρ; and (j–l) for the V_s-only reference. The V_s models are laterally more homogeneous than in Profile A, consistent with the weaker lateral variation seen in the raw field data. Inversions involving V_p again produce shallow high- and low-velocity anomalies, which disappear when ρ is included, highlighting parameter trade-offs. The ρ models remain essentially homogeneous across all cases.*

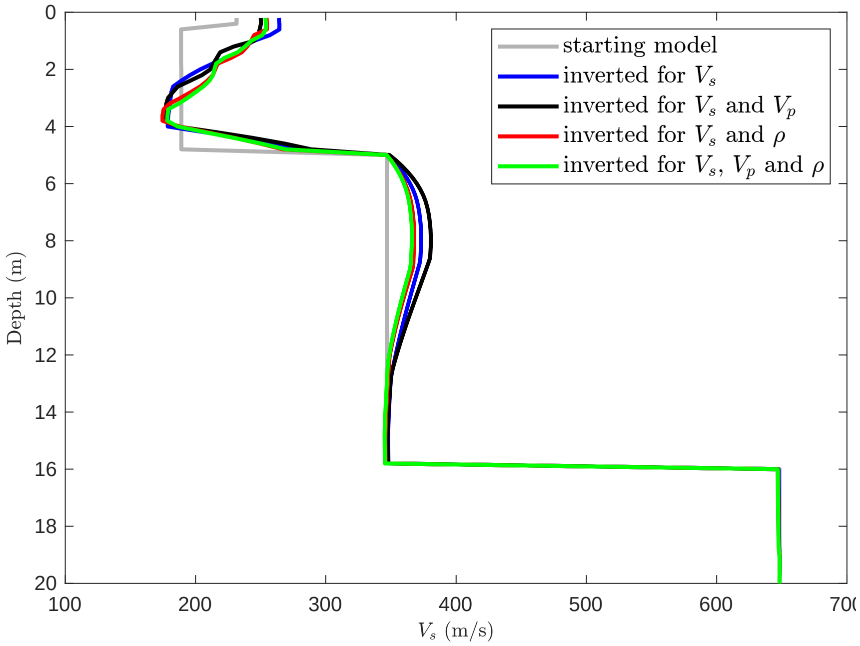

Figure 6.14: *Depth profiles of shear-wave velocity at the distance of 20 m of Profile A comparing starting (gray solid line) and inverted (solid colored) for different parameterizations. Panels (a–c) show V_s, V_p, and ρ for the V_s–V_p inversion; (d–f) for V_s–ρ; (g–i) for V_s–V_p–ρ; and (j–l) for the V_s-only case. In all cases, the near-surface low-velocity zone ($V_s \approx 200$ m/s) is recovered, underlain by a sharp increase to 350–650 m/s. V_p updates show localized anomalies (e.g., a block of elevated velocity at 10–17 m depth) that are suppressed when ρ is included.*

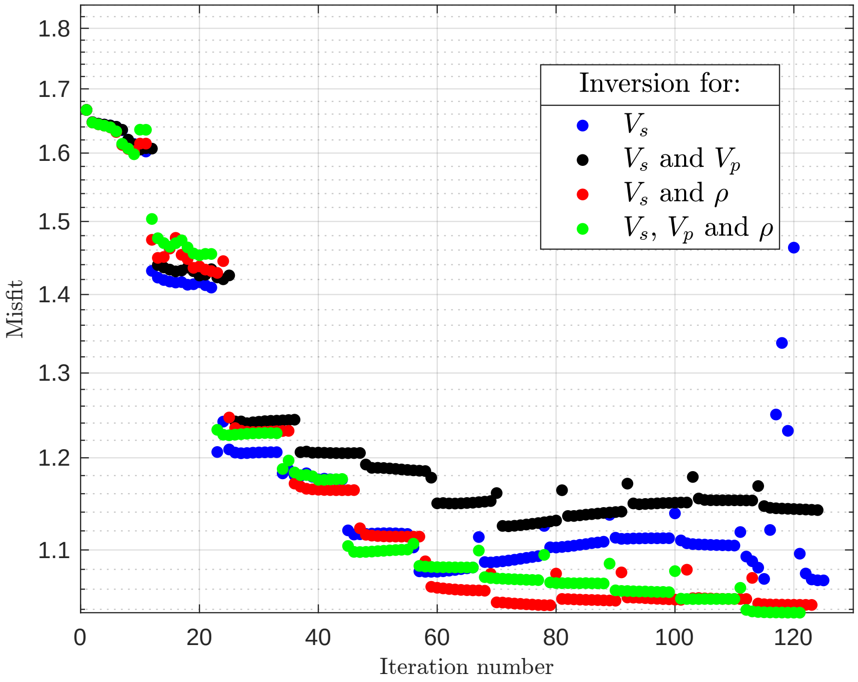

Figure 6.15: *Evolution of the misfit during Profile B inversions for the four parameterizations. The V_s-only inversion converges most smoothly, while the V_s–ρ case achieves the lowest final misfit but shows stronger oscillations. The V_s–V_p and V_s–V_p–ρ curves overlap closely, indicating that V_p updates are not supported by the data. Overall, the misfit behavior confirms that V_s dominates the inversion, with only limited amplitude sensitivity to ρ and negligible constraint on V_p.*

Figure 6.16: *Observed (gray) and synthetic (colored) vertical-component seismograms for Profile B after 77 iterations. Blue lines correspond to the V_s-only inversion, black to V_s–V_p, red to V_s–ρ, and green to V_s–V_p–ρ. All models reproduce the dispersive Rayleigh wavetrain, but there is no systematic improvement when V_p or ρ are included in addition to V_s. The close agreement across parameterizations confirms that the V_s field is robustly constrained, whereas V_p and ρ remain weakly sensitive.*

6.3 Starting-model sensitivity (V_s-only inversion)

To evaluate sensitivity to the initial parameterization, is also considered an alternative V_s starting model with velocities increasing linearly with depth (Figures 6.17b and 6.21b). This model is not part of the baseline results but is used here to test robustness against the choice of starting model. Because full-waveform inversion s a non-linear optimization problem, the recovered solution may depend strongly on the initial model. An unrealistic starting model may drive the inversion into a local minimum, whereas a geologically reasonable one increases the likelihood of a meaningful result. To test this effect, repeated the inversions for both Profile A and Profile B using two different starting models: (i) the four-layer model derived from dispersion analysis (baseline) and (ii) a gradient model with linearly increasing V_s. All other inversion parameters were kept identical, ensuring that any differences in outcome can be attributed solely to the choice of starting model.

6.3.1 Profile A

Figure 6.20 shows the two alternative starting models used to test sensitivity: the four-layer V_s model from dispersion-curve inversion (Section 6.1) and a gradient model constructed by linear interpolation between the minimum and maximum velocities of the layered model. Both were combined with constant V_p (1440 m/s) and ρ (1880 g/cm^3) background model and subjected to the same inversion workflow. The final inverted models (Figure 6.18) converge toward very similar velocity structures despite the different starting assumptions. In both cases, a near-surface low-velocity layer of $\sim$200 m/s in the upper 3–5 m is recovered, underlain by a sharp increase to 200–400 m/s with depth. Minor local differences are visible: the layered starting model produces slightly sharper shallow contrasts, whereas the gradient starting model smoother transitions. These variations are small compared to the overall consistency. Depth profiles (Figure 6.18) confirm that the key features are recovered independently of the starting model, differing mainly in the smoothness of the shallowest layers. The misfit evolution (Figure 6.19) supports this robustness: both inversions show steady reduction with nearly identical final values, offering no basis to prefer one starting model over the other. This underlines that numerical convergence alone does not guarantee geological validity. The comparison of observed–synthetic seismograms (Figure 6.20) further demonstrates that both inversions reproduce the Rayleigh wave-train and amplitude decay equally well, with only minor residuals in later arrivals. In summary, for the Profile A results indicate that the inversion result is stable with respect to the choice of starting model. Both the layered and gradient starting models converge to the same essential velocity structure, recover the near-surface low-velocity zone, and provide satisfactory fits to the observed data. This robustness indicates that the FWI strategy is not overly sensitive to the specific form of the initial V_s model.

6.3.2 Profile B

To test whether the robustness observed in Profile A also holds for Profile B, repeated the starting-model sensitivity analysis with the same two the four-layer V_s model derived from dispersion curves (Section 6.21b) and a gradient model spanning the same velocity range. As before, V_p and ρ were fixed at 1440 m/s and 1880 kg/m^3, and the inversion workflow was unchanged. This allows a direct comparison of how strongly the results depend on the initial parameterization. The final 2D models (Figure 6.5) show that both starting models converge toward nearly identical V_s structures. The same near-surface low-velocity layer and subsequent velocity increase with depth are recovered in both cases. Compared to Profile A, the distribution in Profile B appears more laterally homogeneous, consistent with expectations from the raw field data, which already indicated stronger

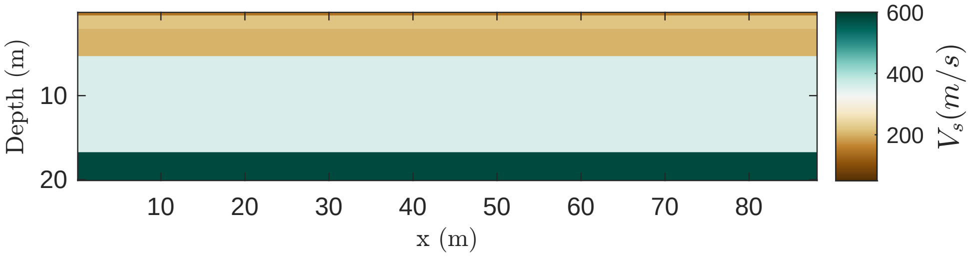

***(a)** four layer V_s starting model*

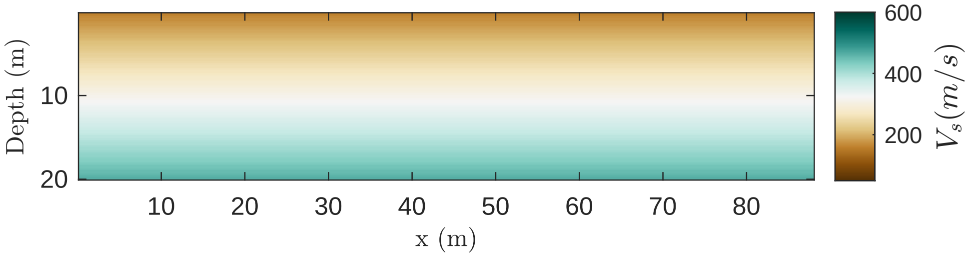

***(b)** Gradient V_s starting model*

***Figure 6.17:** Starting and final model for Profile A in the V_s-only inversion. Panel (a) shows the initial parameterization: a four-layer V_s model derived from dispersion-curve analysis. Panel (b) displays the gradient V_s starting model.*

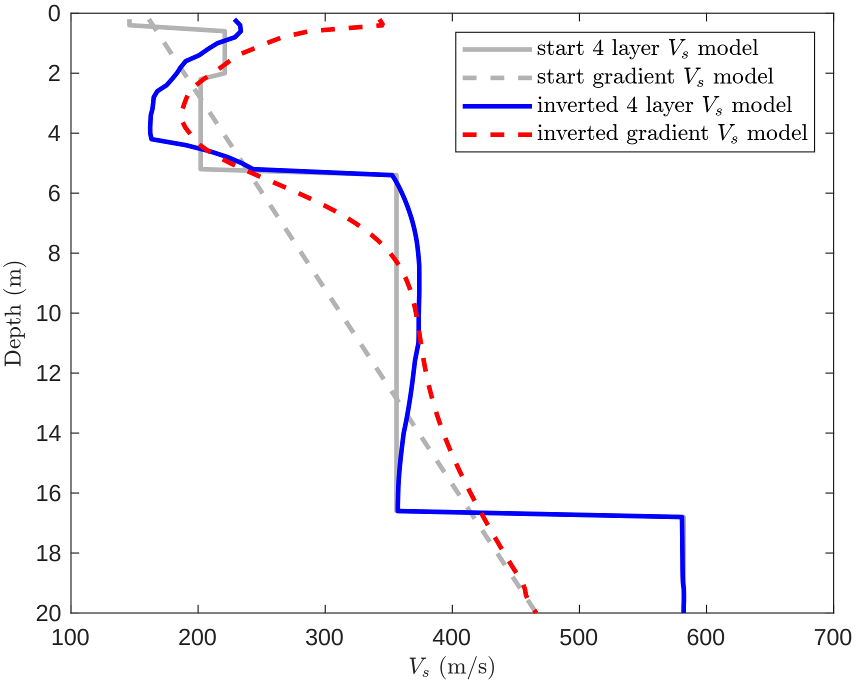

***Figure 6.18:** Comparison of V_s depth profiles, for Profile A using the four-layer and gradient starting models. Both inversions resolve the same low-velocity layer in the top 3–5 m and the gradual increase to 600–700 m/s at depth, differing only in the degree of smoothness in the shallowest part.*

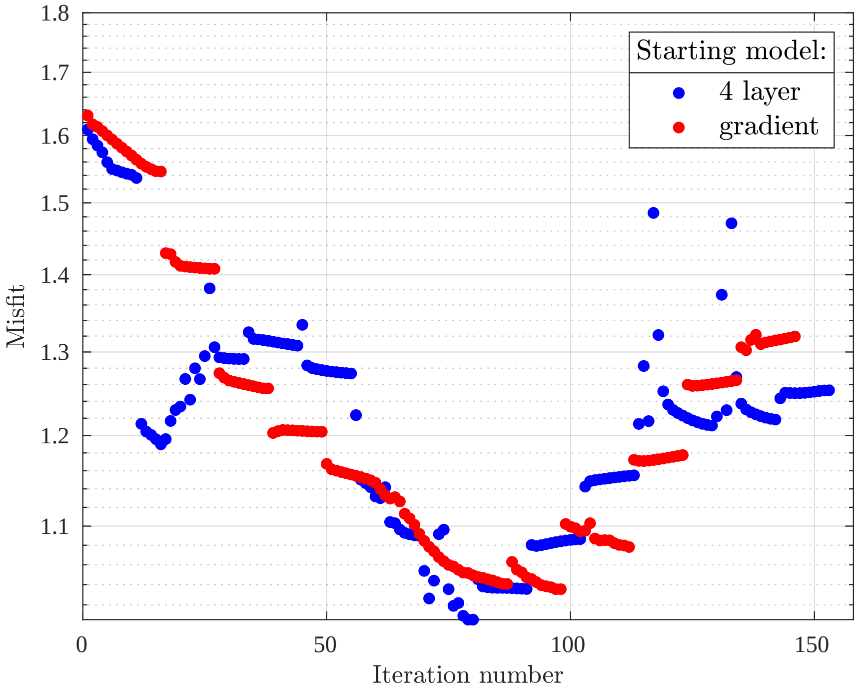

Figure 6.19: *Misfit evolution for Profile A using different starting models. Both the layered and gradient converge to very similar final misfit values, confirming that the inversion performance is largely independent of the chosen starting model.*

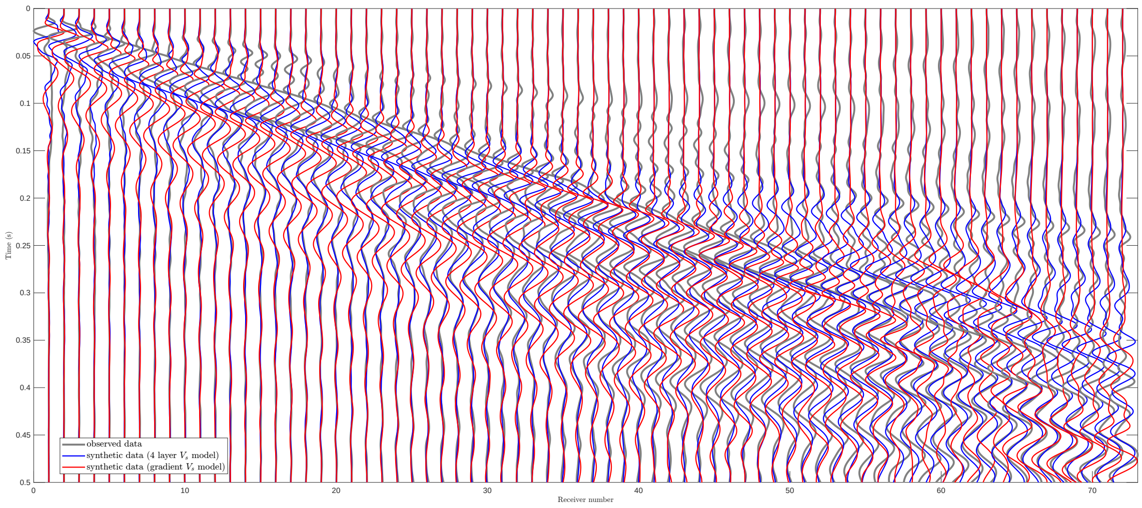

Figure 6.20: *Comparison of observed (gray) and synthetic (colored) seismograms for Profile A, showing the first shot after inversion with different starting models. Both final models reproduce the dispersive Rayleigh-wave wave train and the amplitude decay across the spread, indicating that the data fit is not strongly affected by the choice of starting parameterization.*

lateral variations along Profile A. Depth profiles at 20 m offset (Figure 6.22) confirm this result. Both inversions yield almost identical curves, differing only in the smoothness of the shallowest layers. The misfit evolution (Figure 6.23) likewise shows stable convergence with nearly indistinguishable final values, confirming that the inversion is not sensitive to the choice of starting model. The data-fit comparison (Figure 6.24) further demonstrates that both inversions reproduce the dispersive Rayleigh wavetrain and amplitude decay equally well, with residuals limited to later arrivals and coda energy. Overall, the inversion results for Profile B is stable with respect to the starting model. The consistency across both lines increases confidence that the recovered velocity structures represent robust geological features rather than artifacts of the initial parameterization. Compared to Profile A, the velocity differences between the two starting models in Profile B are smaller and occur mainly at greater depths.

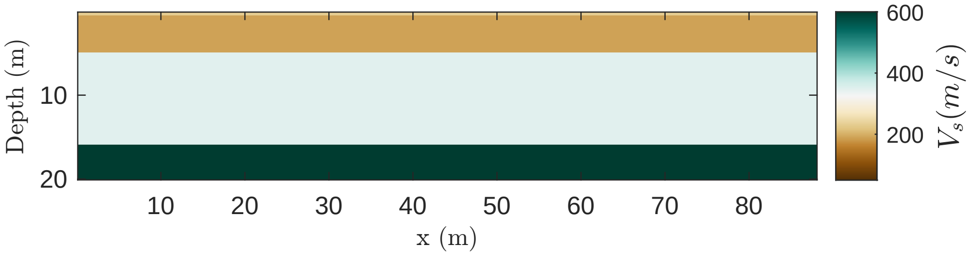

(a) *four layer V_s starting model*

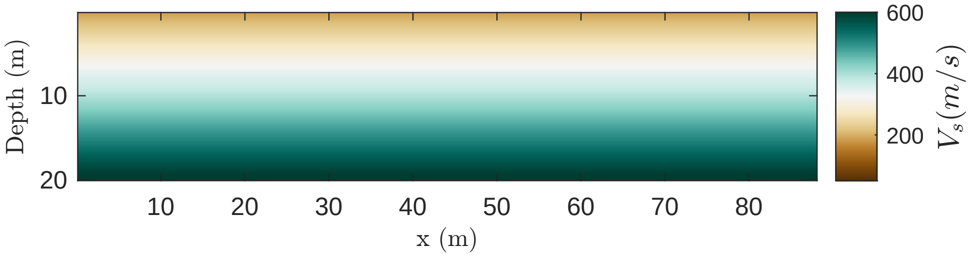

(b) *Gradinet V_s starting model*

Figure 6.21: *Starting and final model for Profile B in the V_s-only inversion. Panel (a) shows the initial parameterization: a four-layer V_s model derived from dispersion-curve analysis. Panel (b) displays the gradient V_s starting model.*

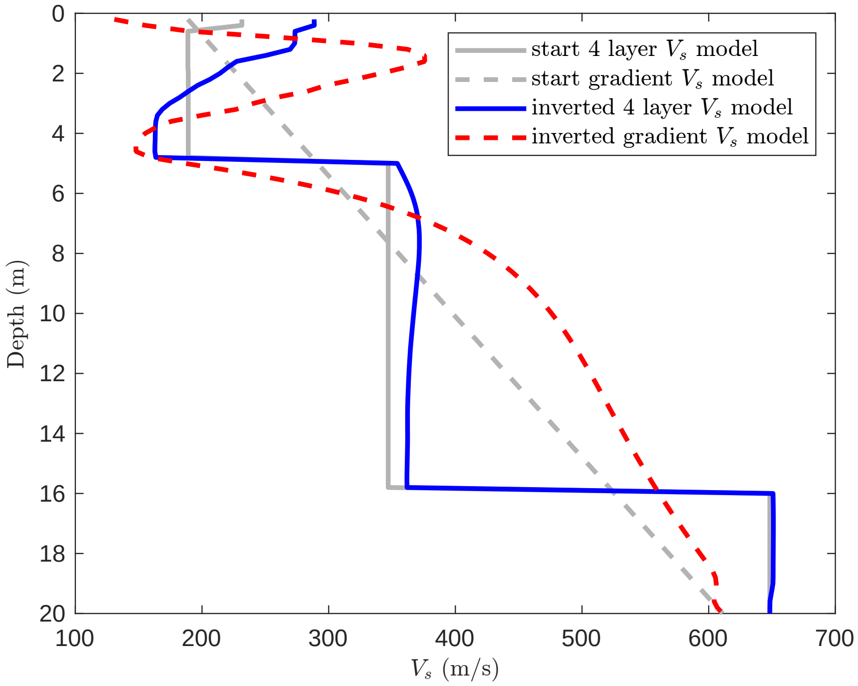

Figure 6.22: *Comparison of starting and inverted V_s depth profiles, Profile B. The inversion resolves a low-velocity layer of about 200 m/s in the top 3–5 m, underlain by a sharp increase to 400–500 m/s, improving on the smooth starting model. At greater depth, the inverted profile approaches 600–700 m/s, consistent with the gravel-rich unit described in*

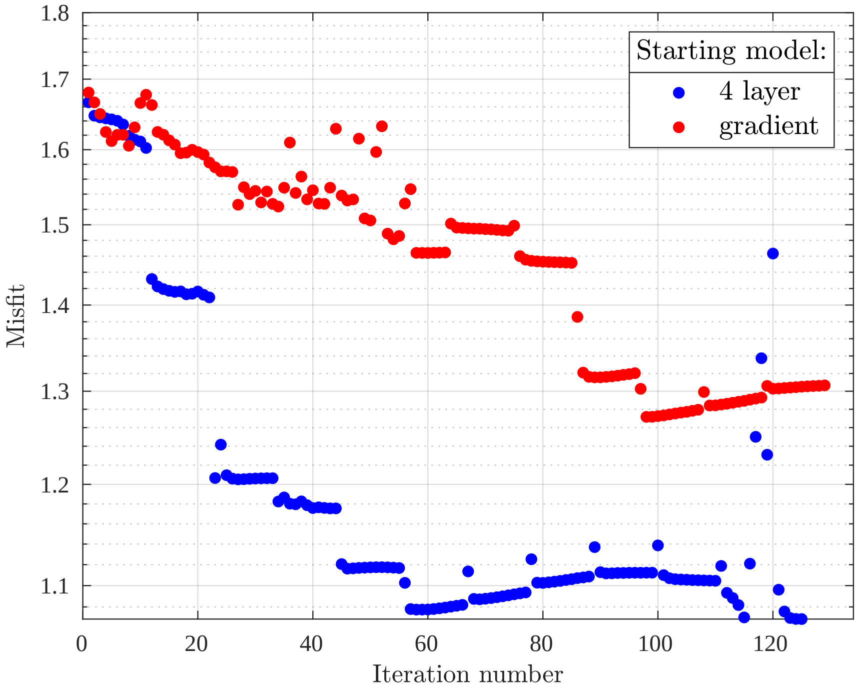

Figure 6.23: *Evolution of the misfit during V_S-only inversion for Profile B. The misfit decreases rapidly in the initial stages and stabilizes after about 60 iterations, indicating convergence of the inversion. The multi-scale frequency strategy ensures that long wavelengths are fit first, followed by finer-scale structure at higher frequencies.*

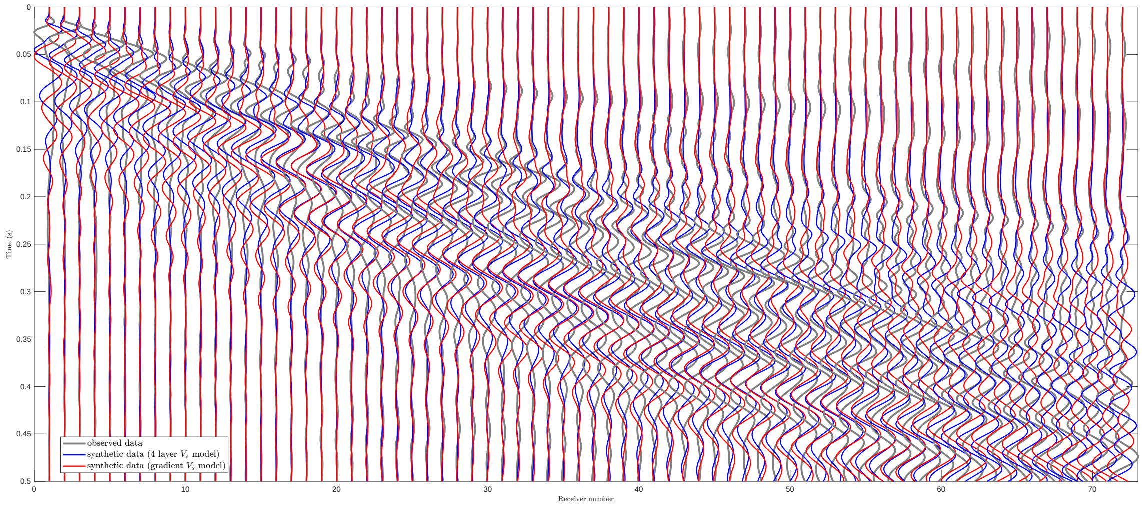

Figure 6.24: *Comparison of observed and synthetic vertical-component seismograms for Profile B after V_s-only inversion.The good agreement across the receiver spread, particularly in the dispersive Rayleigh wavetrain, confirms that the recovered V_s model provides an adequate explanation of the recorded data. Residual differences at large offsets are attributed to noise and unmodeled small-scale heterogeneity.*

6.4 Cross-profile consistency at the intersection

An important measure of robustness is whether independent inversions recover consistent structures at the same location. Since Profiles A and B were inverted separately, with different acquisition geometries and independently derived starting models, the intersection of two profiles provides a natural benchmark for cross-validation. If the velocity structures agree at the intersection, confidence in both the inversion workflow and the geological plausibility of the recovered models is considerably strengthened. Figure 6.25 shows the V_s depth profiles from Profiles A and B at the intersection. Both the starting models (dashed lines) and the inverted results (solid) are displayed. The inverted profiles agree well: in each case, a near-surface low-velocity layer of around 200 m/s extends through the upper 3–5 m, followed by a sharp increase to 400–500 m/s. This contrast corresponds to the gravel-rich unit described in Chapter 3. At greater depths, both profiles show a gradual increase in velocity toward 600–700 m/s, with only minor differences. This agreement across the entire depth range indicates that the main features of the subsurface structure are reliably recovered. The starting models, by contrast, show noticeable differences in the shallowest 0–2 m. This outcome is expected, as the models were constructed independently from dispersion-curve inversions. Surface-wave dispersion inversion is inherently non-unique: it is most sensitive to average shear velocities with depth, while its ability to resolve the very near surface is limited. Factors such as local coupling conditions, small-scale heterogeneity, and the choice of regularization can therefore lead to differences in the reconstructed shallow velocities. These variations do not necessarily reflect real geological changes, but rather the limited resolving power of dispersion analysis in this depth range. Importantly, the full-waveform inversion corrects for these discrepancies, converging toward a consistent low-velocity layer across both profiles. Overall, the cross-profile comparison provides a strong internal consistency check. It shows that, although the dispersion-derived starting models differ in the shallowest layers, the FWI results converge toward stable and geologically plausible solutions. This analysis demonstrates that the inversion strategy applied in this study leads to reliable and reproducible models, reducing the dependence on non-unique starting conditions and increasing confidence in the interpretations presented in the following discussion.

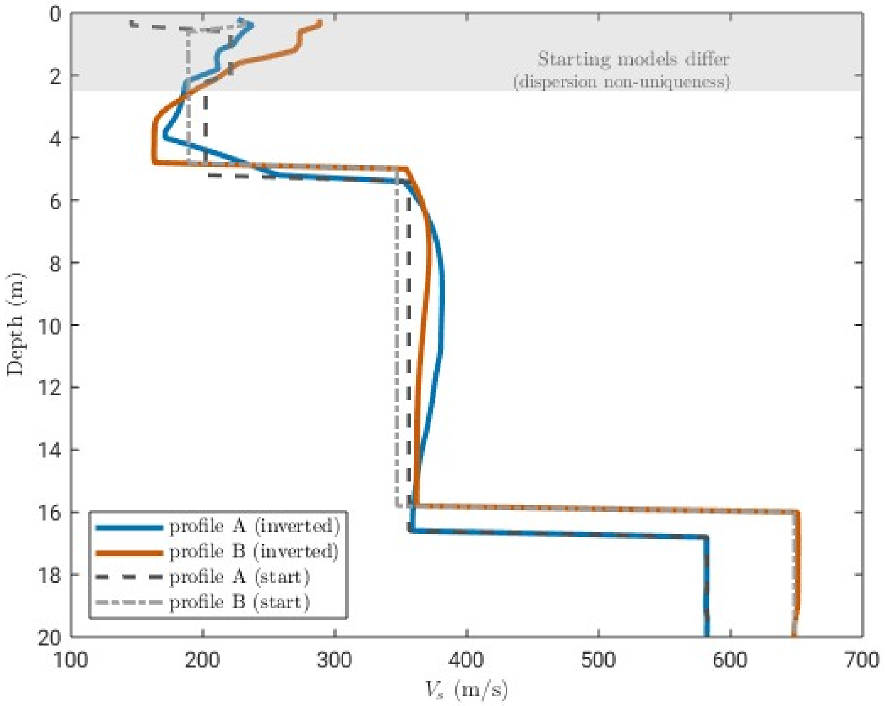

Figure 6.25: *Comparison of V_s depth profiles at the intersection of Profiles A and B. Starting models (dashed line) and inverted results (solid lines) are shown. Both inversions consistently recover a low-velocity layer of ∼150 m/s within the upper 3–5 m, underlain by a sharp increase to 400–500 m/s. The starting models differ slightly in the shallowest meters, reflecting the limited near-surface resolution and non-uniqueness of dispersion-curve inversion. Nevertheless, the FWI results converge toward a consistent structure, demonstrating cross-profile agreement and supporting the reliability of the recovered near-surface model.*

6.5 Discussion

The results across both lines are internally consistent and align with the theoretical sensitivity of Rayleigh waves. Four main outcomes emerge.

(1) V_s is robustly constrained and reproducible. For both profiles, the V_s-only inversions converge stably to geologically plausible models (Figs. 6.1, 6.5). The near-surface low-velocity zone (LVZ; 200 m/s in the upper 3 m to 5 m) and the subsequent rise to 400 to 500 m/s, with a gradual increase toward $600\,\mathrm{m\,s^{-1}}$ to $700\,\mathrm{m\,s^{-1}}$ at depth, are consistently recovered. Misfits reduce monotonically to ∼1.1 (Figs. 6.3, 6.7), and overlays of observed and synthetic seismograms confirm that the dispersive Rayleigh wavetrain is well reproduced (Figs. 6.4, 6.8). The cross-profile intersection test (Fig. 6.25) further supports repeatability: independently inverted lines agree within the full 0 m to 10 m depth and inversion models are just the starting models deeper than 10 m.

(2) Multi-parameter inversions do not add robust structure beyond V_s. Across parameterizations, including ρ can lower the objective function slightly (particularly on Profile B), but the corresponding density updates remain small and non-systematic, offering no interpretable structure (Figs. 6.9, 6.13). Allowing V_p to vary introduces localized anomalies, such as central high-velocity blocks and shallow low-velocity zones, which disappear when ρ is added—evidence of trade-offs between weakly constrained parameters. Importantly, the misfit curves for V_s–V_p and V_s–V_p–ρ often overlap (Fig. 6.11), and the corresponding data fits are indistinguishable (Figs. 6.12, 6.16). Thus, for Rayleigh-wave-dominated data, V_s provides the robust information, whereas V_p and ρ do not.

(3) Sensitivity of inversion to the starting model Using either a layered or a smooth-gradient starting model leads to nearly identical final V_s models (Figs. 6.17b–6.22); the misfit evolution converges similarly (Figs. 6.19, 6.23), and comparisons between observed and synthetic data show only minor differences (Figs. 6.20, 6.24). These results suggest that the four-layer starting model with sharp boundaries is the closest representation of reality and is geologically plausible, given that the test site is a man-made gravel pit. For Profile B, however, the results from the two starting models diverge slightly more than for Profile A, particularly at greater depths, indicating that the inversion is somewhat more sensitive to the choice of starting model in this case. For Profile B, however, the inversion exhibits stronger depth-dependent variability and a somewhat different misfit evolution compared to Profile A, indicating greater sensitivity to the choice of starting model in this case. A plausible explanation for the contrasting misfit behavior of the two profiles is that they sample different subsurface conditions. The raw datasets already show that one line is laterally more homogeneous, which favors stable inversion and smoother models, whereas the other line crosses stronger lateral variations, making the inversion more sensitive to the starting model and more prone to variability at depth. These differences may also reflect directional anisotropy or 3D structural effects that are not fully accounted for in the present 2D inversion.

(4) Implications for the UVT reference model and future work. For the UVT project, a reliable elastic reference model is needed primarily to validate the vibroseis source signature and to invert for the emitted force. The present results provide a stable and repeatable V_s model that fulfils this requirement. However, V_p and ρ are not constrained by Rayleigh waves alone in this setting. If a fully elastic reference is required, we recommend augmenting the dataset with body-wave information (first arrivals, shallow reflections) and/or multi-component recordings, and then repeating the joint inversion with parameter-scale preconditioning tailored to balance sensitivities.

Chapter 7

Summary

Aim and approach

The primary aim of this thesis was to build a reliable near-surface elastic reference model for the Herrenknecht test site in support of the Urban Vibro Truck (UVT) project. Two perpendicular active-source profiles were inverted using two-dimensional elastic full-waveform inversion (FWI) of Rayleigh-wave data. The study evaluated (i) the stability of shear-wave velocity recovery, (ii) the added value of multiparameter inversions including density and P-wave velocity, and (iii) the sensitivity of results to starting models. Synthetic tests complemented the field study to separate methodological from data limitations. Three main conclusions can be drawn:

1. **Shear-wave velocity (V_s) is recovered robustly and repeatably.** Both profiles converged to consistent velocity structures, resolving a shallow low-velocity zone underlain by progressively faster layers. Cross-profile comparisons confirmed that these results are not profile-specific but reflect the true subsurface. A plausible explanation for the contrasting misfit behavior of the two profiles is that they sample different subsurface conditions. The raw datasets already indicate that one line is laterally more homogeneous, which favors stable inversion and smoother models, whereas the other line crosses stronger lateral variations, making the inversion more sensitive to the starting model and more prone to variability at depth. These differences may also reflect directional anisotropy or 3D structural effects that are not fully accounted for in the 2D inversion.
2. **Multi-parameter inversions do not provide stable additional information.** Allowing density or P-wave velocity to vary reduced the misfit in some cases but did not yield interpretable structures. Local anomalies disappeared once parameter trade-offs were accounted for. Rayleigh-wave data alone therefore constrain V_s, but not V_p or ρ.
3. **The inversion is insensitive to the starting model within reasonable bounds.** Both layered and smooth gradient starts converged to nearly identical final V_s models up to 10 m. This indicates that, with a multi-scale frequency strategy, the recovered structure is controlled by the data rather than the starting assumptions.

Implications

The V_s models produced here fulfill the UVT requirement for a stable elastic reference that can be used to validate source signatures and estimate forces. However, V_p and ρ cannot be constrained by Rayleigh-waves alone; a fully elastic model requires complementary body-wave or multi-component data. Synthetic tests confirmed these limits, showing that misfit reduction is not a sufficient criterion for multiparameter recovery.

Limitations and outlook

This study was restricted to two-dimensional viscoelastic modeling and Rayleigh-wave sensitivity. Residual mismatches likely reflect 3D heterogeneity and unmodeled attenuation. Depth penetration was limited to 10 m by the available frequency content. Future work should combine Rayleigh and body-wave information, exploit multi-component data, and introduce parameter-scaling strategies to reduce trade-offs.

Closing statement

This thesis demonstrates that elastic FWI of Rayleigh waves can deliver a robust near-surface shear-wave velocity model that is consistent across independent profiles. Multi-parameter extensions do not add reliable structure under the present data conditions. The results provide a solid V_s reference for the UVT project and point the way towards more complete elastic models through integrated acquisition and inversion strategies.

Appendix A

Source time function inversion

This appendix provides the complete source-time function inversion (STFI) settings and additional diagnostics used in the inversions.

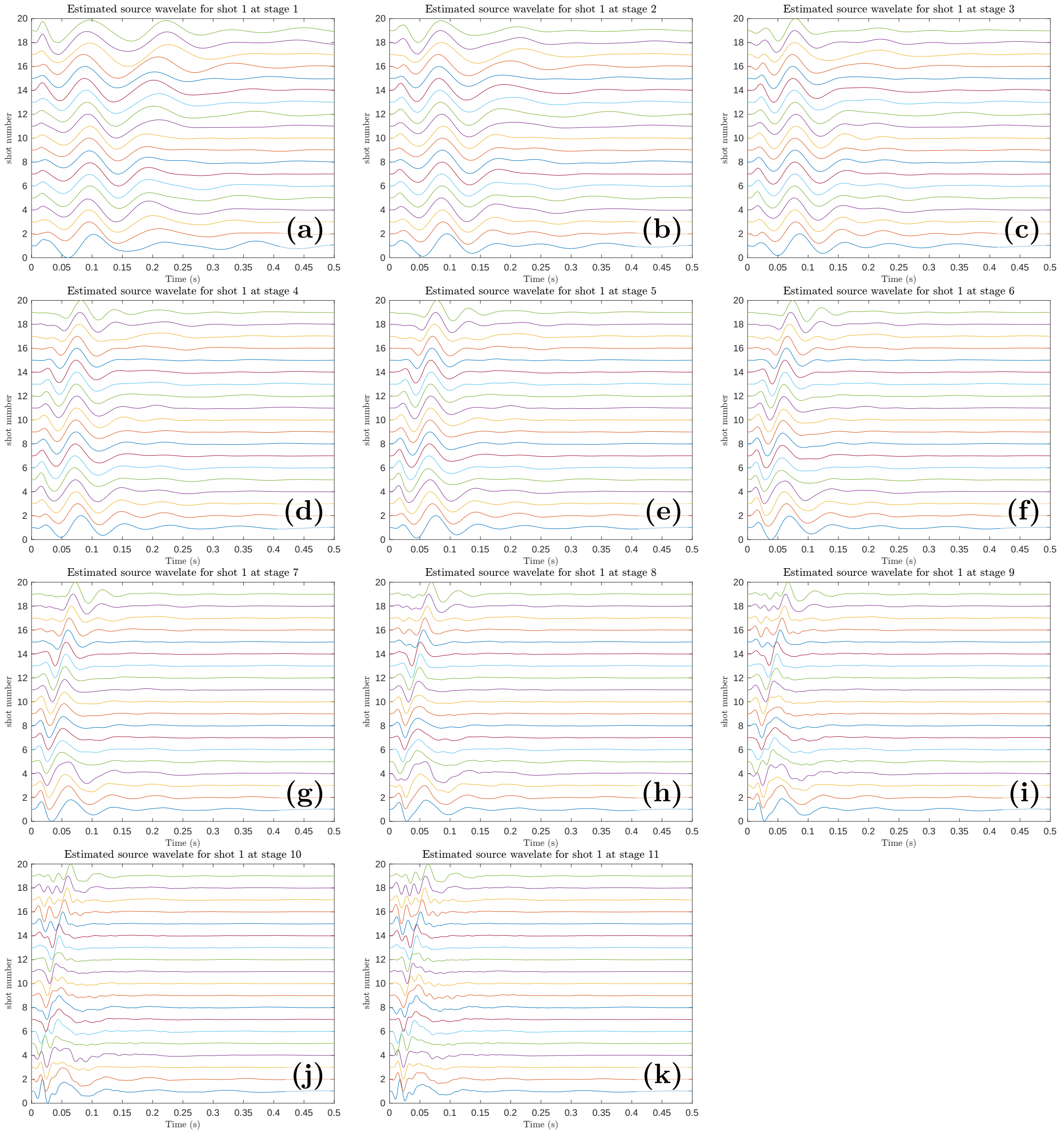

Figure A.1: *STFI across frequency stages. Each panel shows the stage-specific comparison used to update the source signature within the multi-scale FWI workflow for Profile A.*

Appendix B

Software

B.1 IFOS2D

Listing B.1: *Configuration JSON file*

```
{
"Domain Decomposition" : "comment",
"NPROCX" : "8",
"NPROCY" : "5",

"FD order" : "comment",
"FDORDER" : "4",
"MAXRELERROR" : "0",

"2-D Grid" : "comment",
"NX" : "440",
"NY" : "100",
"DH" : "0.2",

"Time Stepping" : "comment",
"TIME" : "0.5",
"DT" : "5.0e-05",

"Source" : "comment",
"SOURCE_SHAPE" : "2",
"SOURCE_SHAPE values: ricker=1;fumue=2;from_SIGNAL_FILE=3" : "comment",
"SOURCE_SHAPE           SIN**3=4;Gaussian_deriv=5;Spike=6" : "comment",
"SIGNAL_FILE" : "./ormsby/ormsby.dat",
"SOURCE_TYPE" : "3",
"SOURCE_TYPE values (point_source): explosive=1;force_in_x=2" : "comment",
"SOURCE_TYPE                    force_in_y=3;rotated_force=4" : "comment",
"SRCREC" : "1",
"SRCREC values : read source positions from SOURCE_FILE=1" : "comment",
"SRCREC values : PLANE_WAVE=2" : "comment",
"SOURCE_FILE" : "./source/sources_realdata.dat",
"RUN_MULTIPLE_SHOTS" : "1",

"Acoustic Computation" : "comment",
"ACOUSTIC" : "0",

"Model" : "comment",
"READMOD" : "0",
"MFILE" : "model_true/smoothmodel_firstpro_true_it_0",

"Free Surface" : "comment",
```

```
"FREE_SURF" : "1",

"PML Boundary" : "comment",
"FW" : "10",
"VPPML" : "1700.0",
"FPML" : "31.25",
"BOUNDARY" : "0",
"npower" : "4.0",
"k_max_PML" : "1.0",

"Receiver" : "comment",
"SEISMO" : "1",
"READREC" : "1",
"REC_FILE" : "./receiver/rec_realdata.dat",
"REFRECX, REFRECY" : "0.0 , 0.0",

"Seismograms" : "comment",
"NDT" : "1",
"SEIS_FORMAT" : "1",
"SEIS_FILE" : "su/realmeasured_data",

"Q-approximation" : "comment",
"L" : "3",
"FL1" : "0.5211",
"FL2" : "7.6660",
"FL3" : "72.6774",
"TAU" : "0.0966",

"General inversion parameters" : "comment",
"ITERMAX" : "400",
"DATA_DIR" : "su/realmeasured_data/realdata",
"PARAMETERIZATION" : "1",
"FORWARD_ONLY" : "0",
"ADJOINT_TYPE" : "2",
"MISFIT_LOG_FILE" : "LOG_test2.dat",

"Inversion for parameter starting from iteration" : "comment",
"INV_RHO_ITER" : "400",
"INV_VP_ITER" : "400",
"INV_VS_ITER" : "0",

"Output of inverted models" : "comment",
"INV_MODELFILE" : "model/smoothmodel_firstpro_true",
"nfstart" : "1",
"nf" : "1",

"Output of gradients" : "comment",
"JACOBIAN" : "jacobian/realdata/jac_realdata",
"nfstart_jac" : "1",
"nf_jac" : "1",

"Workflow" : "comment",
"USE_WORKFLOW" : "0",
"FILE_WORKFLOW" : "workflow.txt",

"Approx. Hessian" : "comment",
"EPRECOND" : "0",
"EPSILON_WE" : "0.005",
```

```
"EPRECOND_ITER" : "0",

"Gradient-Method" : "comment",
"GRAD_METHOD" : "1",
"LBFGS_STEP_LENGTH" : "1",
"N_LBFGS" : "5",

"Wolfe Condition" : "comment",
"WOLFE_CONDITION" : "1",
"WOLFE_NUM_TEST" : "5",
"WOLFE_TRY_OLD_STEPLENGTH" : "1",

"Misfit Definition" : "comment",
"LNORM" : "7",
"LNORM values: L1 norm=1, L2 norm=2, Cauchy=3, SECH=4," : "comment",
"LNORM values: Glob. correl.=5, L2 norm with time windowing=6" : "comment",
"NORMALIZE" : "0",
"DTINV" : "15",

"Step length estimation" : "comment",
"EPS_SCALE" : "0.04",
"STEPMAX" : "4",
"SCALEFAC" : "5.0",
"TESTSHOT_START , TESTSHOT_END , TESTSHOT_INCR" : "1 , 5 , 2",

"Termination of the programmme" : "comment",
"PRO" : "0.002",

"Definition of inversion for source time function" : "comment",
"INV_STF" : "1",
"PARA" : "fdlsq:tshift=0.0:exp=0.5:waterlevel=0.01",
"N_STF" : "10",
"N_STF_START" : "1",
"TAPER_STF" : "0",
"TRKILL_STF" : "1",
"TRKILL_FILE_STF" : "./trace_kill/trace_kill",
"TRKILL_STF_OFFSET" : "1",
"TRKILL_STF_OFFSET_LOWER , TRKILL_STF_OFFSET_UPPER" : "0 , 5",
"TRKILL_STF_OFFSET_INVERT" : "0",

"Trace killing" : "comment",
"TRKILL" : "1",
"TRKILL_FILE" : "./trace_kill/trace_kill",
"TRKILL_OFFSET" : "1",
"TRKILL_OFFSET_LOWER , TRKILL_OFFSET_UPPER" : "0 , 5",

"Frequency filtering during inversion" : "comment",
"TIME_FILT" : "1",
"FC_START" : "5.0",
"F_LOW_PASS_END" : "70.0",
"F_LOW_PASS_INCR" : "10.0",
"ORDER" : "4",
"FREQ_FILE" : "frequencies.dat",
"WRITE_FILTERED_DATA" : "1",

"Minimum number of iteration per frequency" : "comment",
"MIN_ITER" : "10",
```

```
"Definition of gradient taper geometry" : "comment",
"SWS_TAPER_CIRCULAR_PER_SHOT" : "1",
"SRTSHAPE" : "1",
"SRTRADIUS" : "3.0",
"FILTSIZE" : "1",
"SWS_TAPER_FILE" : "0",

"Upper and lower limits for model parameters" : "comment",
"VPUPPERLIM" : "2420",
"VPLOWERLIM" : "100",
"VSUPPERLIM" : "5000",
"VSLOWERLIM" : "100",
"RHOUPPERLIM" : "5000",
"RHOLOWERLIM" : "0",

"Definition of smoothing the models vp and vs" : "comment",
"MODEL_FILTER" : "1",
"FILT_SIZE" : "3",

"Verbose mode" : "comment",
"VERBOSE" : "0"
}
```

B.2 QuillBot (grammar checker)

Parts of the text in this thesis were revised using QuillBot to correct grammar and improve clarity. The tool was employed solely for language editing; no scientific results, interpretations, or analyses were generated by AI.

Bibliography

Achenbach, J. (2012). *Wave propagation in elastic solids.* Elsevier.

Aki, K. and Richards, P. G. (2002). *Quantitative seismology.*

Athanasopoulos, N., Manukyan, E., Maurer, H., and Bohlen, T. (2020). "Time-frequency windowing in multiparameter elastic FWI of shallow seismic wavefield". *Geophysical Journal International* 222.2, pp. 1164–1177.

Boaga, J., Foti, S., and Socco, L. V. (2013). "Multi-component analysis of surface waves". *Geophysical Prospecting* 61.4, pp. 762–775.

Bunks, C., Saleck, F. M., Zaleski, S., and Chavent, G. (1995). "Multiscale seismic waveform inversion". *Geophysics* 60.5, pp. 1457–1473.

De Moura, C. A. and Kubrusly, C. S. (2013). "The courant–friedrichs–lewy (cfl) condition". *AMC* 10.12, pp. 45–90.

Groos, L., Schäfer, M., Forbriger, T., and Bohlen, T. (2013). "2D full waveform inversion of shallow-seismic Rayleigh waves: Modelling and inversion strategies". *Geophysics* 78.6, R211–R222.

Groos, L., Schäfer, M., Forbriger, T., and Bohlen, T. (2014). "The role of attenuation in 2D full-waveform inversion of shallow-seismic body and Rayleigh waves". *Geophysics* 79.6, R247–R261.

Groos, L., Schäfer, M., Forbriger, T., and Bohlen, T. (2017). "Application of a complete workflow for 2D elastic full-waveform inversion to recorded shallow-seismic Rayleigh waves". *Geophysics* 82.2, pp. 1–9.

Kalita, M., Operto, S., and Virieux, J. (2019). "Target-oriented elastic full-waveform inversion of Rayleigh waves: An application to shallow seismic imaging". *Geophysics* 84.2, R145–R162.

Köhn, D., De Nil, D., Kurzmann, A., Przebindowska, A., and Bohlen, T. (2012). "On the influence of model parametrization in elastic full waveform tomography". *Geophysical Journal International* 191.1, pp. 325–345.

Komatitsch, D. and Martin, R. (2007). "An unsplit convolutional perfectly matched layer improved at grazing incidence for the seismic wave equation". *Geophysics* 72.5, SM155–SM167.

Levander, A. R. (1988). "Fourth-order finite-difference P-SV seismograms". *Geophysics* 53.11, pp. 1425–1436.

Liu, H.-P., Anderson, D. L., and Kanamori, H. (1976). "Velocity dispersion due to anelasticity; implications for seismology and mantle composition". *Geophysical Journal International* 47.1, pp. 41–58.

Luo, Y. and Schuster, G. T. (1991). "Wave-equation traveltime inversion". *Geophysics* 56.5, pp. 645–653.

Métivier, L., Allain, A., Brossier, R., Mérigot, Q., Oudet, E., and Virieux, J. (2018). "Optimal transport for mitigating cycle skipping in full-waveform inversion: A graph-space transform approach". *Geophysics* 83.5, R515–R540.

Nazarian, S., Stokoe II, K. H., and Hudson, W. R. (1983). *Use of spectral analysis of surface waves method for determination of moduli and thicknesses of pavement systems.* 930.

Nocedal, J. and Wright, S. J. (2006). *Numerical optimization.* Springer.

Orozco, M. C. (2004). *Inversion method for spectral analysis of surface waves (SASW).* Georgia Institute of Technology.

Pan, W. and Wang, Y. (2019). "Elastic full waveform inversion of surface waves for near-surface imaging". *Geophysical Journal International* 217.2, pp. 1304–1318.

Park, C. B., Miller, R. D., Xia, J., and Ivanov, J. (2007). "Multichannel analysis of surface waves (MASW)—active and passive methods". *The leading edge* 26.1, pp. 60–64.

Plessix, R.-E. (2006). "A review of the adjoint-state method for computing the gradient of a functional with geophysical applications". *Geophysical Journal International* 167.2, pp. 495–503.

Rasho, A. (2025). "Seismic investigation of subsurface structure at the Herrenknecht test site - VS and Q". Master's Thesis. Karlsruhe, Germany: Karlsruhe Institute of Technology.

Tarantola, A. (1984). "Inversion of seismic reflection data in the acoustic approximation". *Geophysics* 49.8, pp. 1259–1266. DOI: 10.1190/1.1441754.

Virieux, J. (1986). "P-SV wave propagation in heterogeneous media: Velocity-stress finite-difference method". *Geophysics* 51.4, pp. 889–901.

Virieux, J. and Operto, S. (2009). "An overview of full waveform inversion in exploration geophysics". *Geophysics* 74.6, WCC1–WCC26.

Wittkamp, F., Athanasopoulos, N., and Bohlen, T. (2019). "Individual and joint 2-D elastic full-waveform inversion of Rayleigh and Love waves". *Geophysical Journal International* 216.1, pp. 350–364.

Acknowledgments

I would like to thank Prof. Dr. Thomas Bohlen for supervision, guidance, and constructive feedback throughout this work. I also thank Prof. Dr. Andreas Rietbrock for serving as second supervisor.

I am grateful to Dr. Laura Gassner for day-to-day advice, technical discussions, and practical help.

Finally, I thank our group's postdoctoral researchers, Dr. Thomas Hertweck and Dr. Lars Houpt, for their feedback during presentations and for reading my draft and providing helpful comments.